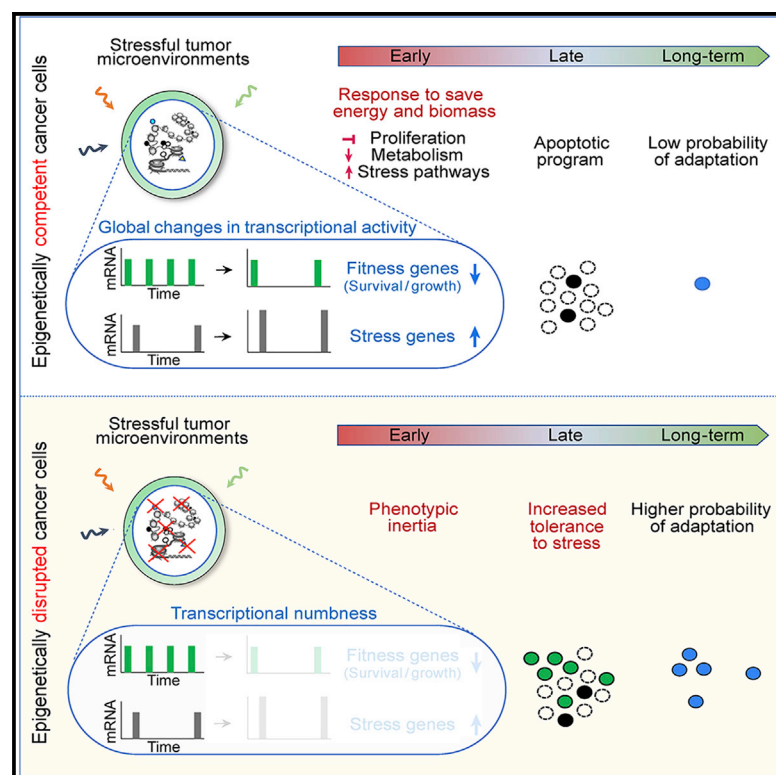# Selective advantage of epigenetically disrupted cancer cells via phenotypic inertia

Graphical abstract

Highlights

- Selection of a disrupted epigenetic regulatory network in evolving human cancers

- Loss of many epigenetic regulators confers broad resistance to environmental stress

- Enhanced fitness of epigenetically disrupted cells is driven by phenotypic inertia

- Defective modulation of transcription rates underpins the stress-tolerant phenotype

Authors

Ioannis Loukas, Fabrizio Simeoni, Marta Milan, ..., Erik Sahai, Vahid Shahrezaei, Paola Scaffidi

Correspondence

paola.scaffidi@crick.ac.uk

In brief

Loukas et al. show that loss of many epigenetic regulators, frequently mutated across cancer types, promote subclone expansion by conferring resistance to stressful environments. Epigenetically disrupted cells fail to efficiently rewire transcription in response to stress, lowering the probability of cell death at early stages and favoring stochastic population adaptation.

CellPress

Article

Selective advantage of epigenetically disrupted cancer cells via phenotypic inertia

Ioannis Loukas,[1,5] Fabrizio Simeoni,[1,5] Marta Milan,[1] Paolo Inglese,[1] Harshil Patel,[2] Robert Goldstone,[2] Philip East,[2] Stephanie Strohbuecker,[2] Richard Mitter,[2] Bhavik Talsania,[1] Wenhao Tang,[3] Colin D.H. Ratcliffe,[4] Erik Sahai,[4] Vahid Shahrezaei,[3] and Paola Scaffidi[1,6,*]

[1]Cancer Epigenetics Laboratory, The Francis Crick Institute, London, UK
[2]Bioinformatics and Biostatistics, The Francis Crick Institute, London, UK
[3]Department of Mathematics, Imperial College London, London, UK
[4]Tumour Cell Biology Laboratory, The Francis Crick Institute, London, UK
[5]These authors contributed equally
[6]Lead contact
*Correspondence: paola.scaffidi@crick.ac.uk
https://doi.org/10.1016/j.ccell.2022.10.002

SUMMARY

The evolution of established cancers is driven by selection of cells with enhanced fitness. Subclonal mutations in numerous epigenetic regulator genes are common across cancer types, yet their functional impact has been unclear. Here, we show that disruption of the epigenetic regulatory network increases the tolerance of cancer cells to unfavorable environments experienced within growing tumors by promoting the emergence of stress-resistant subpopulations. Disruption of epigenetic control does not promote selection of genetically defined subclones or favor a phenotypic switch in response to environmental changes. Instead, it prevents cells from mounting an efficient stress response via modulation of global transcriptional activity. This "transcriptional numbness" lowers the probability of cell death at early stages, increasing the chance of long-term adaptation at the population level. Our findings provide a mechanistic explanation for the widespread selection of subclonal epigenetic-related mutations in cancer and uncover phenotypic inertia as a cellular trait that drives subclone expansion.

INTRODUCTION

Cancers comprise heterogeneous populations of malignant cells characterized by distinct biological properties, which differentially contribute to disease maintenance and progression. The phenotype and properties of each cell are shaped by a combination of genetic, epigenetic, and environmental factors (Marusyk et al., 2012). Genetic intratumor heterogeneity is prevalent across cancers, and many tumors contain spatially separated subclonal populations that evolve following distinct trajectories (Dentro et al., 2021; McGranahan and Swanton, 2017). Evidence of positive selection of fitter subclones exists, with dominant subclonal lineages detected in various cancer types (Vendramin et al., 2021). However, the mechanisms that drive sublclone expansion remain only partially understood. At the pan-cancer level, sublclonal alterations in canonical cancer drivers that promote cancer initiation (e.g., *KRAS*, *TP53*, *CDKN2A*) are present in some patients, but they are relatively rare (Dentro et al., 2021), raising the possibility that distinct mechanisms may drive tumorigenesis and subsequent cancer evolution. Furthermore, only 11% of detected subclones harbor mutations in functionally validated cancer genes, and it has been difficult to identify recurrent, subclonally mutated genes (Dentro et al., 2021). Instead,

classes of genes, such as those involved in the DNA damage response, epigenetic regulators, and splicing factors, are enriched among subclonally mutated genes (Dentro et al., 2021; Jamal-Hanjani et al., 2017). These observations suggest that phenotypic traits induced by disruption of the corresponding biological processes (i.e., genome maintenance and gene expression regulation), rather than specific genotypes, may be selected during cancer evolution.

Epigenetic regulator genes encode proteins involved in the establishment and maintenance of chromatin and DNA methylation landscapes and, as a group, are among the most mutated genes across cancer types (Shen and Laird, 2013; Lawrence et al., 2014). Genetic alterations include translocations that create oncogenic fusion proteins (e.g., MLL fusions in leukemia), hot-spot gain-of-function (GOF) mutations (e.g., EZH2 Y646 substitutions in B cell lymphoma), and loss-of-function (LOF) alterations that affect a wide range of regulators (Shen and Laird, 2013). In contrast to oncogenic alterations, which are highly tissue specific, LOF mutations are often observed across multiple cancer types, with varying recurrence (Shen and Laird, 2013; Lawrence et al., 2014; Mittal and Roberts, 2020). Moreover, while translocations and GOF mutations are typically clonal, in line with an early role in driving carcinogenesis (Bödör
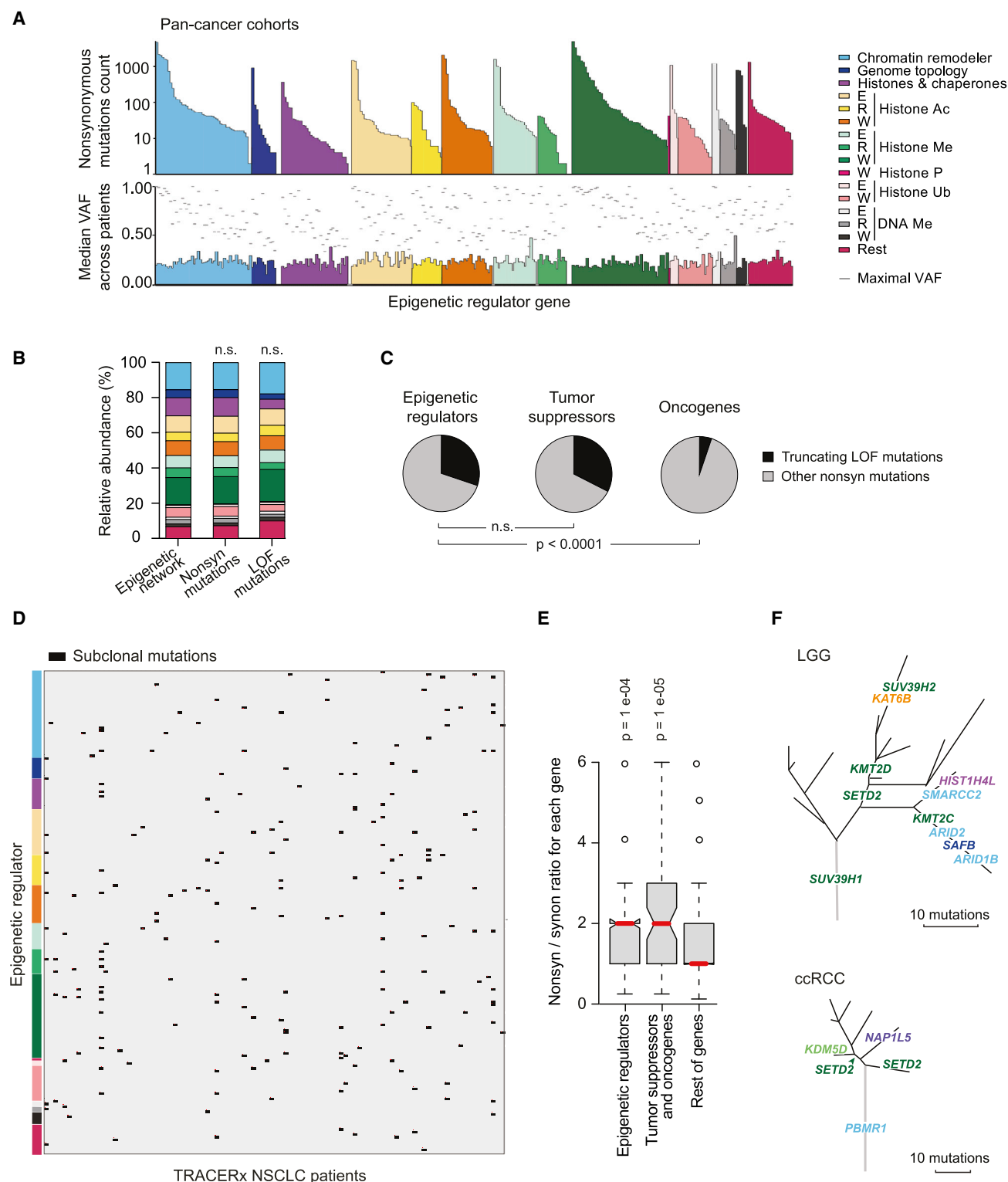
Figure 1. Subclonal mutations disrupting the epigenetic regulatory network in cancer patients

(A) Distribution of nonsynonymous mutations across the indicated functional classes of epigenetic regulators. E, eraser; R, reader; W, writer; Ac, acetylation; Me, methylation; P, phosphorylation; Ub, ubiquitination.

(B) Proportions of mutations across functional classes of epigenetic regulators, compared with the proportions of genes in each class (epigenetic network). n.s., not significant ($p > 0.05$, two-tailed χ^2 test). Legend as in (A).

(C) Fraction of LOF mutations in the indicated groups of genes. p values from two-tailed Fisher's test.

et al., 2013; Nikbakht et al., 2016), LOF mutations can be clonal (e.g., *PBRM1* in clear cell renal cell carcinoma) (Turajlic et al., 2018), be mainly present in emerging subclones (e.g., *SETD2* in various cancers) (Dentro et al., 2021), or exhibit complex patterns (e.g., *ARID1A*), with early inactivation in some contexts (Wiegand et al., 2010; Martincorena et al., 2018) and later, subclonal mutations in others (Dentro et al., 2021). These patterns suggest that loss of epigenetic regulators may play distinct role in tumorigenesis and cancer evolution. Mechanisms underpinning early oncogenic functions have been characterized for some genes, and they often promote transformation by interfering with cellular differentiation (Shen and Laird, 2013). On the other hand, how epigenetic deregulation induced by late mutations further enhances cancer cell fitness and favors subclone expansion within established tumors is poorly understood.

Cancer cell fitness, defined as the number of descendants generated by a malignant cell in a given time frame, is an integrative phenotype that combines long-term proliferative potential and the ability to withstand both cell-intrinsic stress (e.g., genotoxic, proteotoxic, and metabolic stress) and environmental challenges faced during tumor growth. Regional differences in selective pressures such as hypoxia, acidity, limited availability of nutrients, and physical constraints shape the tumor composition by favoring expansion of subpopulations of cells that can withstand those challenges (Junttila and de Sauvage, 2013). The fitness of cancer cells is thus highly dependent on the environment in which they grow and the stress they experience. In this study, we modeled the widespread epigenetic-related mutations observed in patients and examined their impact on cancer cell fitness under stressful conditions typical of the tumor microenvironment.

RESULTS

Selection of a disrupted epigenetic regulatory network during cancer evolution

Recurrently mutated epigenetic regulators identified through unbiased analysis of patient samples belong to diverse functional classes, including chromatin remodelers, histones, histone modifiers, regulators of genome topology, and DNA modifiers (Lawrence et al., 2014). To comprehensively examine the distribution of mutations across the epigenetic regulatory network independently of recurrence at the individual-gene level, we probed the status of more than 300 genes (Table S1) in six pan-cancer datasets available through the cBioPortal (Zehir et al., 2017; Robinson et al., 2017; Miao et al., 2018; Hyman et al., 2018; ICGC/TCGA Pan-Cancer Analysis of Whole Genomes Consortium, 2020; Nguyen et al., 2022; Gao et al., 2013). Overall we identified 60,907 nonsynonymous mutations spread across the whole network, with no functional class being particularly affected (Figures 1A and 1B). As observed in targeted studies, approxi-

mately one-third of these alterations across all classes were truncating LOF mutations, a fraction comparable with that of established tumor-suppressor genes (Figure 1C). At the pan-cancer level, LOF mutations were also prevalent in genes that act as oncogenic drivers in specific cancer types (e.g., *EZH2* in B cell lymphoma; *KMT2A*, *CREBBP*, and *EP300* in leukemia) or that have been linked to context-dependent synthetic lethalities (e.g., *EZH2* in *ARID1A*-deficient cancers [Bitler et al., 2015] and *MEN1* in MLL-driven leukemia [Yokoyama et al., 2005]) (Figures S1A–S1C).

While alterations with high variant allele frequency (VAF) were detected (maximal VAF across patients ≥ 0.5 for 258 genes, Figure 1A), mutations across the epigenetic regulatory network displayed overall low VAF (median VAF <0.3 for 271 genes, Figure 1A), raising the possibility that many tumors may only harbor these alterations in subsets of cells. To directly examine subclonal mutations selected at later stages of tumor evolution, we analyzed 100 non-small cell lung cancer (NSCLC) patients profiled by multiregion sequencing in the TRACERx study (Jamal-Hanjani et al., 2017). Subclonal nonsynonymous mutations in epigenetic regulator genes were prevalent, with 62% of the samples harboring mutations in at least one gene and 130 genes being affected in at least one patient (Figure 1D). These alterations showed a high nonsynonymous/synonymous ratio at the individual-gene level, which suggests their positive selection during tumor growth (Martincorena et al., 2017) (Figure 1E). No gene or functional class was particularly affected, confirming a broad disruption of the network in emerging subclones (Figure 1D). We also interrogated smaller-scale datasets from glioblastoma multiforme (Suzuki et al., 2015) and kidney cancer (Gerlinger et al., 2014) patients, in which detailed phylogenetic trees were reconstructed to identify subclonal mutations selected over time in evolving tumors. Confirming the patterns observed in NSCLC, subclonal mutations affected a range of epigenetic regulators of diverse function, with up to ten alterations independently selected in individual tumors (Figures 1F, S1D, and S1E). These observations suggest that expanded subclones are often characterized by a disrupted epigenetic regulatory network and that mutations in distinct but functionally related proteins may converge into similar favorable phenotypes that are selected during cancer evolution. We therefore searched for cellular traits gained by epigenetically disrupted cells that could explain the mutational patterns observed in patients.

Disruption of the epigenetic regulatory network enhances cell fitness under environmental stress

In physiology, epigenetic mechanisms mediate the cellular response to environmental cues. We therefore asked whether disruption of epigenetic control in cancer cells may affect their interactions with the tumor microenvironment (TME). We selected two cancer types originating from distinct lineages: NSCLC lung

---

(D) Visualization of subclonal mutations affecting epigenetic regulator genes in the TRACERx patient cohort. Genes grouped by functional class. Colors legend as in (A).

(E) Ratio of nonsynonymous over synonymous mutations in individual genes in the indicated groups. N = 190, 65, and 10,025 genes, respectively. Red lines denote median values. p values relative to the rest of the genes from one-tailed Student's t test after random sampling.

(F) Phylogenetic trees visualizing emerging subclones in two tumors. Mutated epigenetic regulator genes identified in the trunk (gray line, clonal mutations) or in the branches (black lines, subclonal mutations) are indicated. Genes color-coded as in (A).

See also Figure S1 and Table S1.
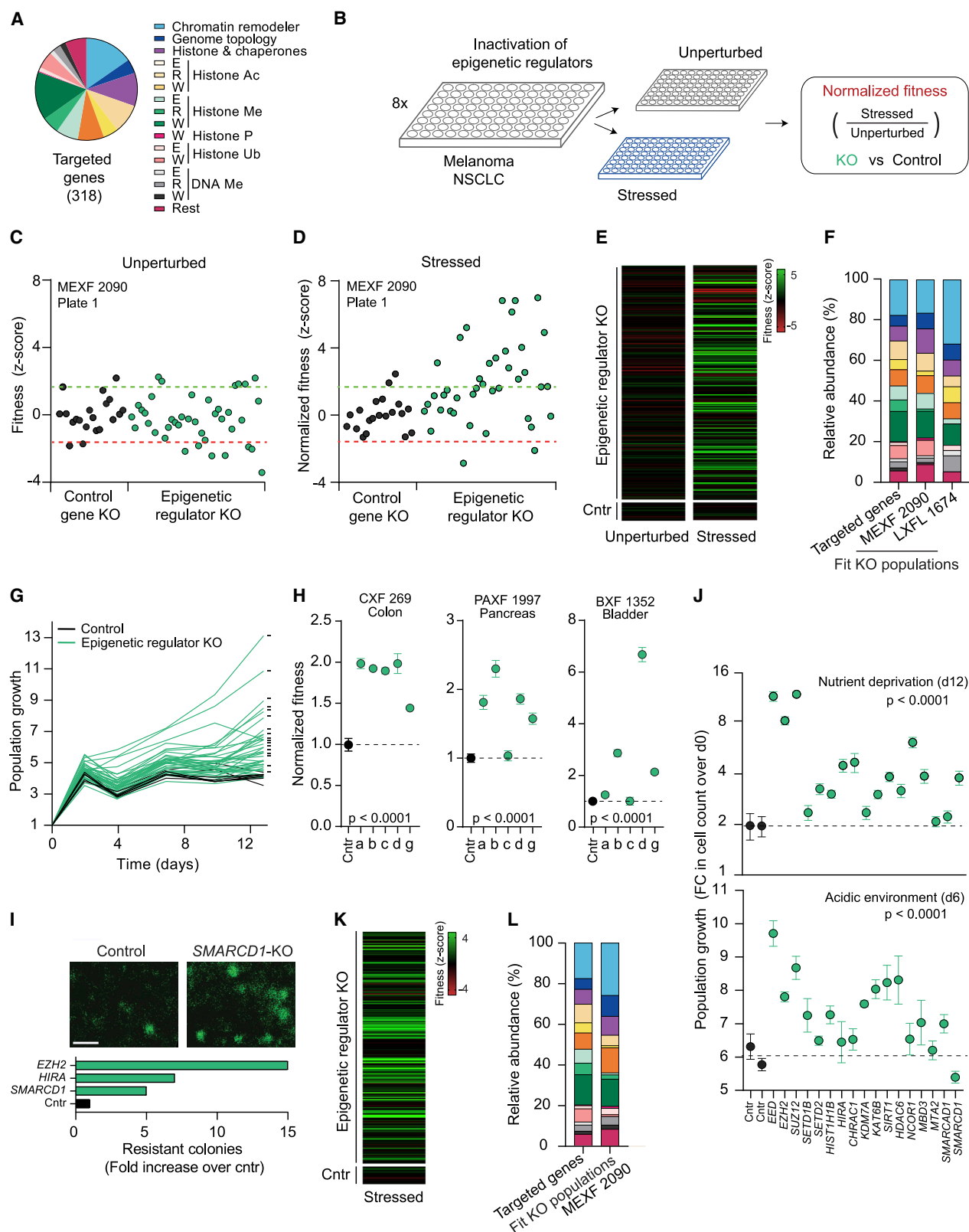
Figure 2. Systematic disruption of the epigenetic regulatory network under stress

(A) Representation of epigenetic functional classes in the CRISPR library.

(B) Schematic of the experimental approach.

carcinoma, of epithelial origin, and melanoma, of melanocytic origin, and obtained cells from respective patient-derived-xenograft (PDX) models (LXFL 1674 and MEXF 2090) (Table S2). The lines express 275 and 278 epigenetic regulators, respectively, and the absence of nonsense mutations in the corresponding genes make them suitable systems to dissect the functional consequences of disrupting the network through experimental gene inactivation (Tables S1 and S2). To minimize genetic heterogeneity, we isolated clonal populations from each model and avoided prolonged culture. A common challenge faced by cancer cells is the reduced availability of nutrients, especially glutamine, in the poorly vascularized TME (Jiang et al., 2019). As expected, both melanoma and lung cancer cells suffered glutamine deprivation, showing a marked decrease in proliferation rate over 3 days (Figure S2A). A comparable effect was also observed when glucose was depleted, indicating that reduced levels of distinct nutrients elicit similar cellular responses (Figure S2B). Despite the apparent cytostasis, the populations were not arrested and reached a steady state where approximately 20% of cycling cells counteracted the death of over 60% of the population (Figure S2C). Prolonged culture revealed the presence of rare stress-resistant cells that reconstituted a growing population (Figure S2D). For both cancer models, replicate populations grown in independent wells showed a range of responses to nutrient deprivation, reflecting varying numbers of resistant colonies (Figure S2E). The stochastic emergence of stress-resistant subpopulations, together with the clonal nature of the lines, suggests a nongenetic basis for the observed phenotype. In agreement, treatment of cells with a panel of epigenetic inhibitors altered the response to stress and promoted resistance (Figures S2F and S2G). Multiple compounds targeting histone modifiers with either repressive or activating functions increased cell fitness under stress, with treated populations showing up to 5-fold more cells than control populations after 9 days (Figures S2F and S2G). Transient inhibition of epigenetic regulators prior to stress was not sufficient to confer the stress-resistance phenotype, which only emerged upon sustained treatment (Figure S2G). The effect was only observed under stress and in fact counteracted a decrease in fitness induced by some drugs in unperturbed conditions (Figures S2F and S2G). Thus, cancer cells with a functional network of epigenetic regulators show a heterogeneous response to nutrient deprivation, with most cells succumbing to stress and a small subset

surviving and being selected over time. This functional heterogeneity can be modulated experimentally, and interference with epigenetic regulation can benefit the cell population under stress.

To mimic on a large scale the widespread LOF mutations observed in patients, we systematically inactivated epigenetic-related genes in both cancer models using an arrayed single-guide RNA (sgRNA) library that targets regulators of chromatin and DNA methylation across 16 functional classes (Figures 2A and 2B; Table S1) (Henser-Brownhill et al., 2017). The approach enables efficient editing in polyclonal populations and is compatible with microscopy-based readouts (Figures S3A and S3B). The aim of this analysis was not to perform a screen but to model the broadly disrupted epigenetic network that is selected in patients and dissect its functional consequences. We generated knockout (KO) cell populations in 96-well format, including on each plate negative control samples in which non-expressed genes were targeted (Figure S3C). We grew cells in either unperturbed conditions or under glutamine deprivation over 7 days, and assessed the stress-specific effect of gene KO on cell fitness (Figures 2B and S3C). To avoid inflated ratios, KO populations with severely compromised fitness under unperturbed conditions were excluded from the analysis, leaving 262 and 250 populations for MEXF 2090 and LXFL 1674, respectively (Table S3). Biological replicates were highly concordant, allowing detection of even mild biological effects (Figure S3D). Assessment of negative controls showed that interwell technical variability was controlled for (Figures 2C, 2D, and S3E). While unperturbed MEXF 2090 KO populations showed fitness values largely within the distribution of negative controls, their fitness was broadly enhanced under stress, with 91 KO populations exhibiting a favorable phenotype (Z score > 1.64) (Figures 2C–2F and Table S3). As expected, targeting of related subunits of protein complexes induced consistent phenotypes, whereas KO of lowly expressed genes had no effect (Figure S3F). Furthermore, validation experiments confirmed accurate detection of enhanced fitness (Figure 2G and Table S3). This analysis also revealed favorable phenotypes that only emerged at later time points, suggesting that the short time frame of the large-scale assays may have underestimated the number of KO populations with enhanced fitness (Figure 2G). We observed both shared and cancer-type-specific effects (Figure S3G and Table S3). Importantly, the stress-resistant phenotype was not restricted to KO

(C and D) Large-scale fitness assay. Results from one of eight plates. Dots, KO populations; green/red lines, Z-score thresholds defining enhanced or decreased fitness.

(E) Heatmap of Z scores for unperturbed (fitness) or nutrient-deprived (normalized fitness) MEXF 2090 cells. The filtered 262 KO populations and control populations (Cntr) from one plate are shown.

(F) Functional classes of genes linked to enhanced fitness under nutrient deprivation. Legend as in (A).

(G) Growth kinetics of 38 KO and five control populations of MEXF 2090 cells. Values are mean from two biological replicates. Dashes denote populations analyzed in (J).
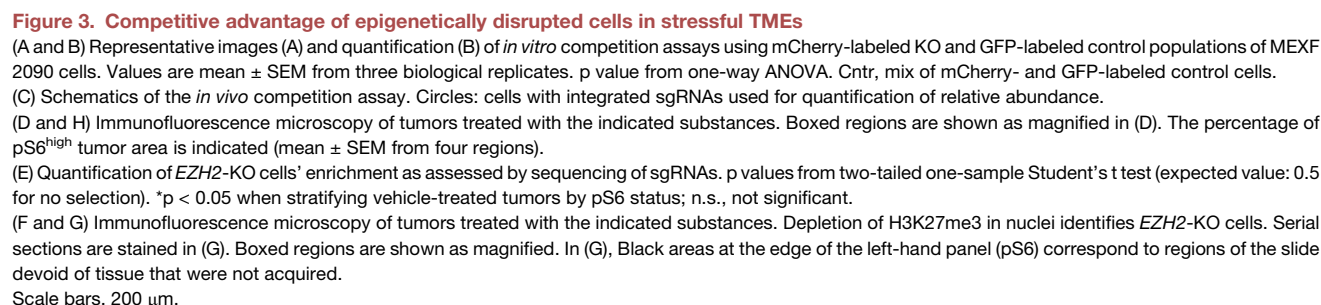
(H) Fitness assays of the indicated models treated with epigenetic inhibitors. Cntr, DMSO; a, RGFP966, b, GSK126, c, tubastatin A; d, quisinostat; g, EX527. Values are mean ± SEM from three biological replicates. p values from one-way ANOVA.

(I) Representative images and quantification of stress-resistant subpopulations. Scale bar, 5 mm.

(J) Fitness assays on selected KO populations of MEXF 2090 cells. Targeted genes are indicated. See STAR Methods regarding endpoint choice. Dashed line denotes mean value from two independent sets of control cells. Values are mean ± SEM from three biological replicates. p values from one-way ANOVA. FC, fold change.

(K) Heatmap of Z scores of normalized fitness for 262 KO populations grown in acidic environment.

(L) Functional classes of genes linked to enhanced fitness in acidic environments. Legend as in (A).

See also Figures S2 and S3; Tables S3 and S4.

Figure 3. Competitive advantage of epigenetically disrupted cells in stressful TMEs

(A and B) Representative images (A) and quantification (B) of *in vitro* competition assays using mCherry-labeled KO and GFP-labeled control populations of MEXF 2090 cells. Values are mean ± SEM from three biological replicates. p value from one-way ANOVA. Cntr, mix of mCherry- and GFP-labeled control cells.

(C) Schematics of the *in vivo* competition assay. Circles: cells with integrated sgRNAs used for quantification of relative abundance.

(D and H) Immunofluorescence microscopy of tumors treated with the indicated substances. Boxed regions are shown as magnified in (D). The percentage of pS6[high] tumor area is indicated (mean ± SEM from four regions).

(E) Quantification of *EZH2*-KO cells' enrichment as assessed by sequencing of sgRNAs. p values from two-tailed one-sample Student's t test (expected value: 0.5 for no selection). *p < 0.05 when stratifying vehicle-treated tumors by pS6 status; n.s., not significant.

(F and G) Immunofluorescence microscopy of tumors treated with the indicated substances. Depletion of H3K27me3 in nuclei identifies *EZH2*-KO cells. Serial sections are stained in (G). Boxed regions are shown as magnified in (G). In (G), Black areas at the edge of the left-hand panel (pS6) correspond to regions of the slide devoid of tissue that were not acquired.

Scale bars, 200 μm.

populations defective in a specific molecular function but was shared across all layers of epigenetic regulation in both cancer models (Figure 2F), with patterns resembling the distribution of LOF mutations observed in patients (Figures 1A and 1B). Notably, 89% and 84% of the inactivated genes that conferred enhanced fitness in MEXF 2090 and LXFL 1674 cells, respectively, were affected by LOF mutations in pan-cancer cohorts, and 38% and 32% were subclonally mutated in the TRACERx cohort. Within the subset of epigenetic regulators with an established role in cancer (An et al., 2016), 52% were associated with the stress-resistance phenotype, including genes often mutated in expanded subclones (e.g., ARID1A and SETD2) (Table S4). KO of other frequently inactivated genes such as KDM6A, KMT2C/D, or CTCF did not enhance cell fitness under stress, suggesting that their loss benefits cancer cells via alternative mechanisms (Table S4). The stress-resistant phenotype of epigenetically disrupted cells was not restricted to melanoma and NSCLC, and cells derived from PDX models of colon, pancreatic, and bladder cancer also exhibited enhanced fitness under stress upon pharmacological interference with multiple epigenetic regulators (Figure 2H). As observed with genetic inactivation and in agreement with the absence of recurrent subclonal mutations in patients (Dentro et al., 2021), we detected both shared and model-specific effects. Thus, independently of context-specific effects of individual genes, the consequences of broadly disrupting the epigenetic regulatory network are conserved across multiple cancer types.

To begin to characterize the stress-resistant phenotype, we selected KO populations that showed varying degrees of enhanced fitness (Figure 2G, dashes) and belonged to various classes of regulators. Increased percentages of proliferating cells and lower percentages of apoptotic cells 3 days after nutrient deprivation suggested that more cells in the population survived and continued to proliferate under stress (Figure S3H). In agreement, clonogenic assays showed a higher number of independent stress-resistant subpopulations after 12 days (Figure 2I). Thus, the enhanced fitness of KO populations results from an increased frequency of surviving cells shortly after stress.

To exclude that the observed phenotypes were due to a decreased dependency of epigenetically disrupted cells on glutamine, we challenged MEXF 2090 cells with another type of stress often faced by cells during tumor growth: hypoxia-induced acidification of the TME (Yoo et al., 2020). More than 60 KO populations were resistant to both types of stress (Figure 2J and Table S3), and acidity-resistant phenotypes were also shared across all functional classes (Figures 2K and 2L). Since nutrient deprivation and low pH have antithetic consequences on cell metabolism (Yoo et al., 2020), this response is likely not due to alterations in specific molecular pathways but rather to a more general ability to survive in a hostile milieu. Of note, KO populations did not show broadly enhanced fitness in response to DNA-damage-related stress such as hydroxyurea-induced replication defects (median Z score: 0.23 versus 0.74 for nutrient deprivation and acidity) (Table S3), suggesting that disruption of epigenetic control mainly increases the ability of cells to cope with environmental challenges. We conclude that inactivation of numerous and diverse epigenetic regulators converges into a common phenotype that enables cancer cells to survive and proliferate in harsh environments.

Stress-dependent selection of epigenetically disrupted cells in the tumor microenvironment

We then examined the behavior of epigenetically disrupted cells in the presence of competing wild-type cells. Co-culture experiments assessing the previously selected KO populations indicated a broad selection of KO cells under stress (Figures 3A and 3B). We then chose EZH2 as a representative regulator frequently inactivated in cancer (Figure S1B) (Laugesen et al., 2016) and performed in vivo competition assays. Although nutrients and oxygen are often limiting in unperturbed tumors, we induced further deprivation by treatment with bevacizumab, an anti-vascular endothelial growth factor A antibody that inhibits angiogenesis (Ferrara, 2005) (Figure 3C). Reduced levels of phosphorylated S6 ribosomal protein (pS6), a readout of mammalian target of rapamycin (mTOR) activity that correlates with nutrient availability (Sabatini, 2017), indicated that the treatment was effective (Figure 3D). EZH2-deficient cells consistently outcompeted control cells in all bevacizumab-treated tumors, independently of host cell abundance, with samples containing up to 95% of EZH2-KO cells (Figures 3E, S3I, and S3J). Immunostaining of tumor sections confirmed the selection of EZH2 LOF during tumor growth, as most cells were depleted of the EZH2-deposited H3K27me3 mark (Figure 3F). EZH2-KO cells were particularly enriched in pS6-negative tumor regions—those most severely affected by bevacizumab treatment—suggesting that intratumor heterogeneity in the TME influences the expansion of epigenetically disrupted cells (Figure 3G). Vehicle-treated tumors showed a bimodal behavior: tumors exhibiting uniformly high pS6 levels, indicative of a nutrient-rich TME, showed comparable abundance of the two cell populations, whereas EZH2-KO cells outcompeted control cells in tumors showing reduced pS6 levels (Figures 3E and 3H). Thus, basal levels of nutrient deprivation in unperturbed tumors are sufficient to promote the selection of EZH2-KO cells, and this effect is maximized under conditions of enhanced stress. Collectively, the evidence from cellular and mouse models, combined with the prevalence of epigenetic-related subclonal mutations in cancer patients, suggests that the increased ability of epigenetically disrupted cells to withstand environmental stress promotes their selection during cancer evolution.

Disruption of epigenetic control does not promote genetic heterogeneity or cell state transitions

Multiple cellular mechanisms could underpin the stress-dependent selective advantage of epigenetically disrupted cells (Figure 4A). One possibility is that inactivation of chromatin and DNA modifiers may promote genomic instability and generate genetically defined stress-resistant subclones. In this scenario, restoring proper epigenetic control after an initial perturbation would not alter the emerged resistance. To test this possibility, we selected epigenetic inhibitors that confer resistance to stress (Figure S2G) and treated cells to induce reversible deregulation under nutrient deprivation; we assessed cell fitness after 9 days, washed out the drugs, and examined the response after further growth under stress (Figure 4B). At each step, all populations were seeded at identical density as the initial seeding to allow comparison of growth rates across conditions. In all cases, stress-resistant phenotypes were reversed upon compound withdrawal, demonstrating that the observed resistance is not genetically encoded (Figure 4B).
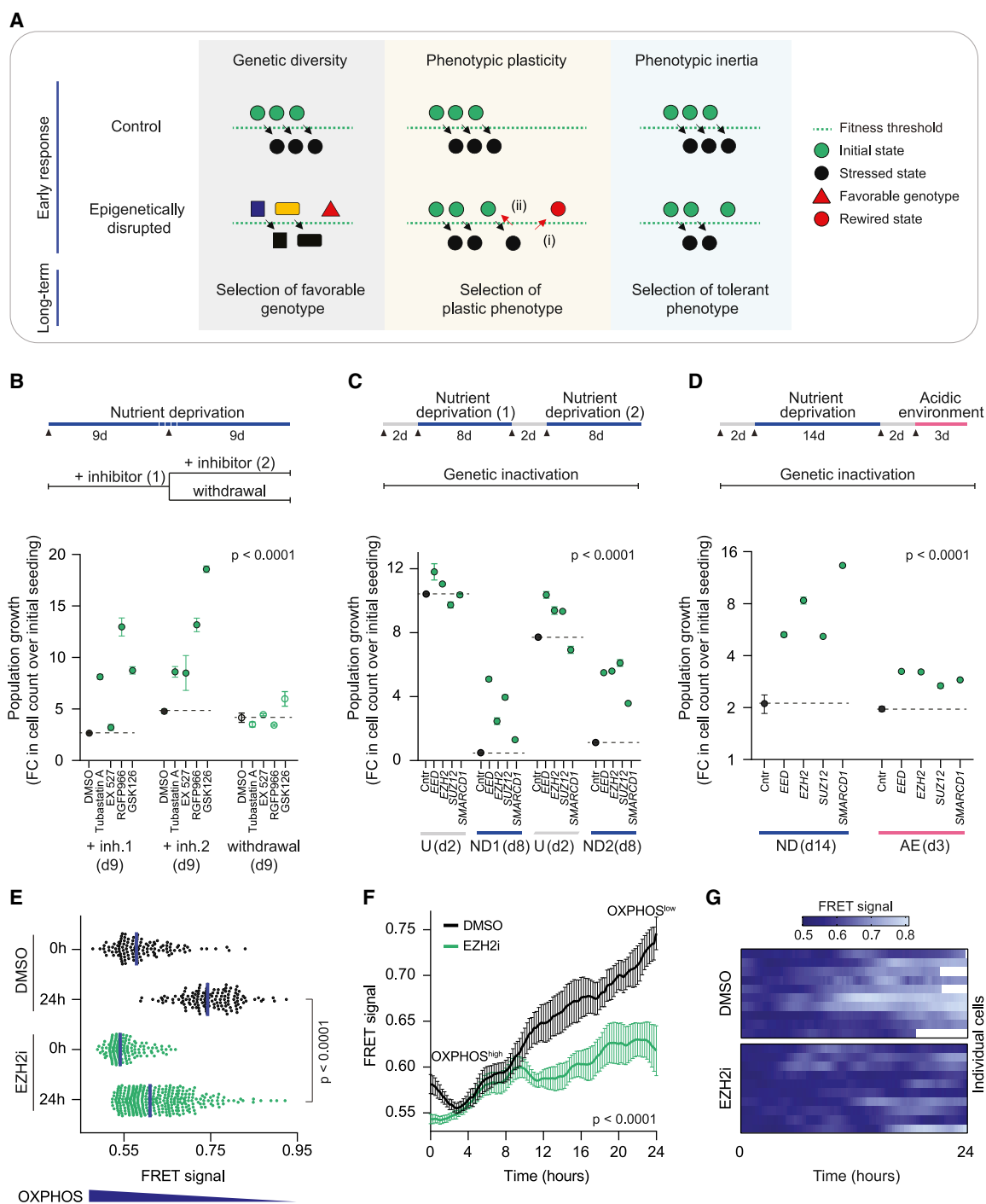
Figure 4. Impaired cell state transitions in epigenetically disrupted cells

(A) Alternative models of stress resistance in epigenetically disrupted cells. (i) Transition to a transcriptionally rewired cellular state after reaching a stressed state; (ii) restoration of the initial state.

(B) Fitness assay on MEXF 2090 cells treated with epigenetic inhibitors following the protocol above. At each seeding (arrowhead), cells were plated at identical density. Values are mean ± SEM from three biological replicates measured at the time point in parentheses. p value from two-way ANOVA at day 18. FC, fold change.

(C and D) Fitness assay on KO populations of MEXF 2090 cells following the protocols above. See STAR Methods for endpoint choice. Values are mean ± SEM from three biological replicates. p values from two-way ANOVA.

(E) Quantification of OXPHOS levels in live MEXF 2090 cells grown under nutrient deprivation using the FRET-based biosensor. N ≥ 126 cells. p value from two-tailed Mann-Whitney U-test.

(F and G) Time-lapse imaging of the indicated cells. Values are mean ± SEM from ten cells, shown separately in the heatmap (G). See STAR Methods for details of basal levels. p value from two-tailed Student's t test calculated at the last time point. White squares: time points where cells could not be tracked.

See also Figure S4 and Table S5.
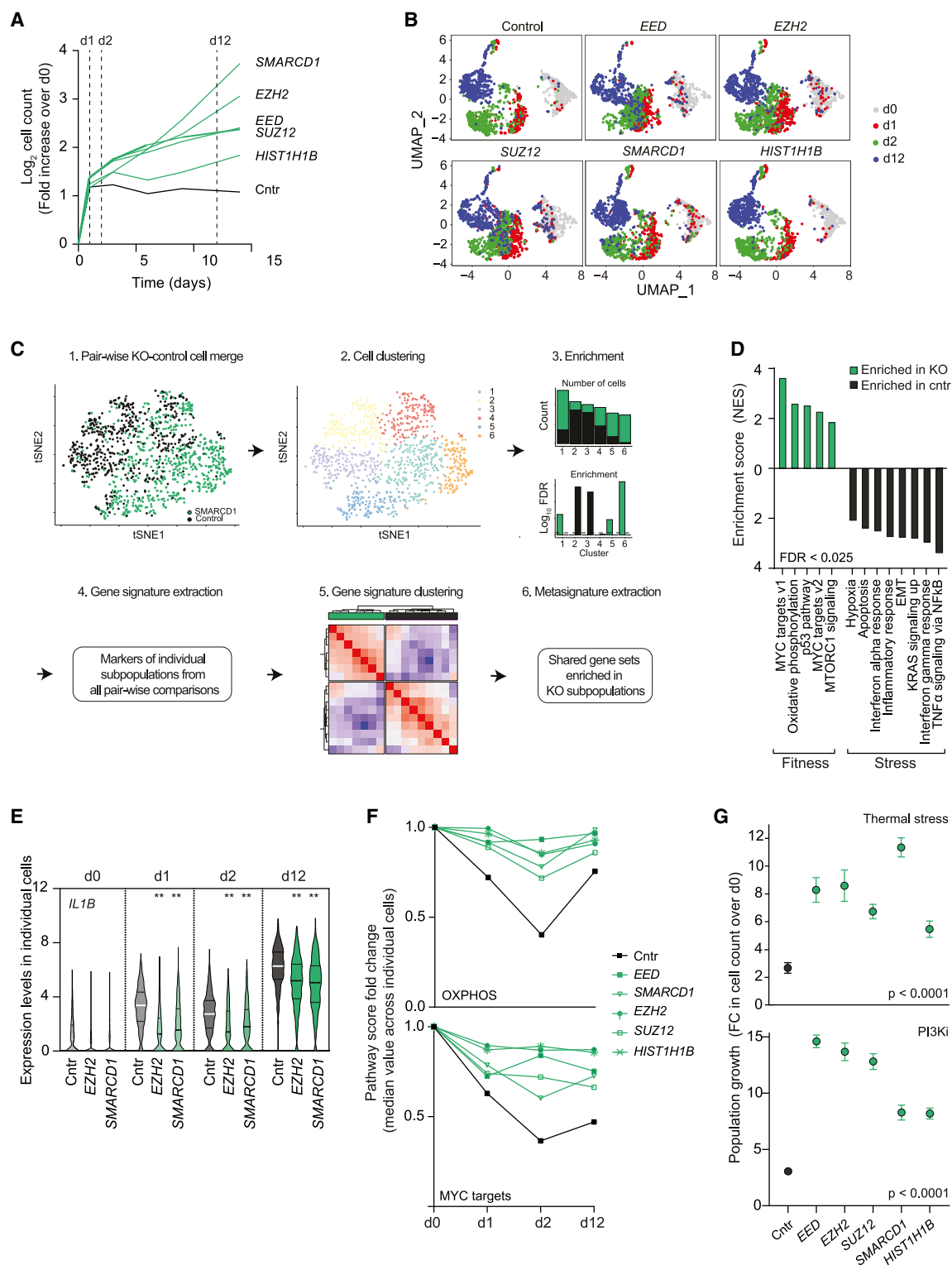
Figure 5. Phenotypic inertia of epigenetically disrupted cells

(A) Growth kinetics of the KO populations analyzed by scRNA-seq under nutrient deprivation.

(B) UMAP dimensionality reduction of the analyzed samples. Plots visualize overall trajectories but underestimate difference with control cells.

(C) Strategy used to dissect phenotypic heterogeneity of cell populations.

(D) Gene set enrichment analysis of identified meta-signatures.

(E) Expression levels of a stress gene in individual cells. Other KO populations show similar trends. **p < 0.01 (Kolmogorov-Smirnov test). N ≥ 270 cells.

(legend continued on next page)

Alternatively, a more permissive epigenetic landscape in KO populations may enhance phenotypic plasticity by favoring transitions between cellular states. This could either entail acquisition of an alternative, favorable cellular state or reversal from a stressed to the initial state (Figure 4A). Consistent with enhanced plasticity, epigenetically disrupted populations reversibly adjusted their growth rate in response to fluctuating environments maintaining consistently higher fitness than control cells, both when facing multiple rounds of nutrient deprivation and when challenged sequentially with distinct types of stress (Figures 4C and 4D).

A third mechanism that we considered, which could also explain the above results, is phenotypic inertia (Figure 4A). If cells are unable to efficiently respond to unfavorable conditions by halting proliferation or activating an apoptotic program, their ability to withstand stress in the short term may be enhanced, increasing the chance of overcoming transient challenges or acquiring secondary adaptive traits. While conceptually antithetic to cellular plasticity, phenotypic inertia would also be consistent with the observed patterns, as the selection of stress-tolerant cells during environmental fluctuations could promote survival and growth of the population under multiple unfavorable conditions (Figures 4C and 4D).

To begin to assess whether epigenetically disrupted cells are plastic or inert, we searched for stress-responsive pathways. We profiled cell transcriptomes prior to stress (day 0 [d0]) and 12 days after nutrient deprivation (d12), comparing control cells and 5 of the 17 KO populations characterized in previous assays. Again, we chose genes that belong to distinct functional classes and that exhibited varying degrees of stress resistance (Figure S4A): the Polycomb repressive complex 2 (PRC2) subunits EZH2, EED, and SUZ12 (Laugesen et al., 2016), the chromatin remodeler SMARCD1 (Carlson and Laurent, 1994), and the linker histone H1B, an integral component of chromatin (Scaffidi, 2016). Control cells responded to stress by downregulating fitness signatures that support cell metabolism, proliferation, and survival, including c-MYC target genes, cell-cycle regulators, mTOR signaling targets, and genes involved in oxidative phosphorylation (OXPHOS) in the mitochondria, the primary source of cellular energy (Figure S4B and Table S5). Concomitantly, stress signatures such as nuclear factor κB or p53 targets and genes driving apoptosis were upregulated (Figure S4B). Similar changes were observed when cells grew in acidic environments, indicating that distinct triggers induce overall similar stressed phenotypes (Figure S4C). In the KO populations, stress-responsive genes were only mildly affected, correlating with the degree of resistance observed in the fitness assays, which confirms a less-stressed phenotype (Figures S4D and S4E). The milder response in KO populations was not due to distinct basal states in unperturbed conditions, as indicated by comparable levels of stress-responsive genes or energy production and unaltered cell-cycle profiles (Figures S4F–S4H). The identification of affected molecular pathways allowed us to test the plasticity model by examining cellular transitions at the single-cell level. Using an established fluorescence resonance energy transfer (FRET)-based biosensor that allows monitoring of metabolic states in living cells (Kondo et al., 2021), we compared relative OXPHOS levels in epigenetically disrupted and control cells. To avoid the presence of unedited cells that would confound the single-cell analysis in KO populations, we selected EZH2 for this analysis and used the specific inhibitor GSK126 (EZH2i) to homogeneously block its function. In agreement with previous reports (Kondo et al., 2021), a low FRET signal indicated high mitochondrial activity, as confirmed by tetramethylrhodamine ethyl ester perchlorate (TMRE) staining, with EZH2i-treated stressed cells displaying higher OXPHOS levels than control cells, as predicted by the RNA sequencing (RNA-seq) analysis (Figures S4I and S4J). One day after nutrient deprivation, control cells acquired a stressed phenotype with markedly decreased OXPHOS levels (Figure 4E). In contrast, most EZH2i-treated cells only displayed minor changes (Figure 4E). To directly examine cellular transitions, we tracked individual cells by time-lapse imaging. While control cells progressively transitioned from a fit OXPHOS^{high} to a stressed OXPHOS^{low} state, EZH2i cells were more static and retained overall higher OXPHOS levels (Figures 4F and 4G). This cell state transition is the immediate response to changing environments and precedes effects on cell proliferation and viability. These observations provide initial evidence that epigenetically disrupted cells do not display enhanced plasticity upon stress and in fact are less responsive to changing environments.

Phenotypic inertia of epigenetically disrupted cells

We then performed single-cell RNA-seq (scRNA-seq) analysis of nutrient-deprived cells at four time points: unperturbed (d0), early stress response (d1, preceding detectable phenotypic changes, and d2, showing initial reduction in fitness but unaffected cell viability), and after selection of resistant cells (d12) (Figure 5A). We minimized technical variability by multiplexing populations and by performing a reversed time course that enabled simultaneous sequencing of all samples (Figure S5A) (see STAR Methods). Quantification of low-quality (LQ) cells, which include highly stressed cells, showed the expected increase at d12, with lower fractions detected in the KO populations (Figures S5B and S5C). Since LQ cells were removed for downstream analysis, detected differences between control and KO populations are an underestimation of the real effects. Control cells showed immediate downregulation of fitness signatures by d2 and a concomitant upregulation of stress pathways, which peaked at d12 (Figures S5D and S5E; Table S5). The late stress response (differentially expressed genes [DEGs] between d2 and d12) also included a partial reversal of stress-induced changes, which confirms the selection of stress-resistant cells (Figures S5F and S5G). Cells from different time points segregated from one another in control cells, as assessed by uniform manifest approximation and projection (UMAP)-based dimensionality reduction, whereas they were less separated in epigenetically disrupted cells and subsets of d1, d2, and d12 cells clustered with d0 populations (Figures 5B, S5H, and S5I).

(F) Relative changes in fitness pathway scores over time upon stress. The median value is plotted for each cell population.
(G) Fitness assays examining control and KO populations of MEXF 2090 cells grown under the indicated types of stress. Values are mean ± SEM from three biological replicates. p values from one-way ANOVA.
See also Figure S5 and Table S5.
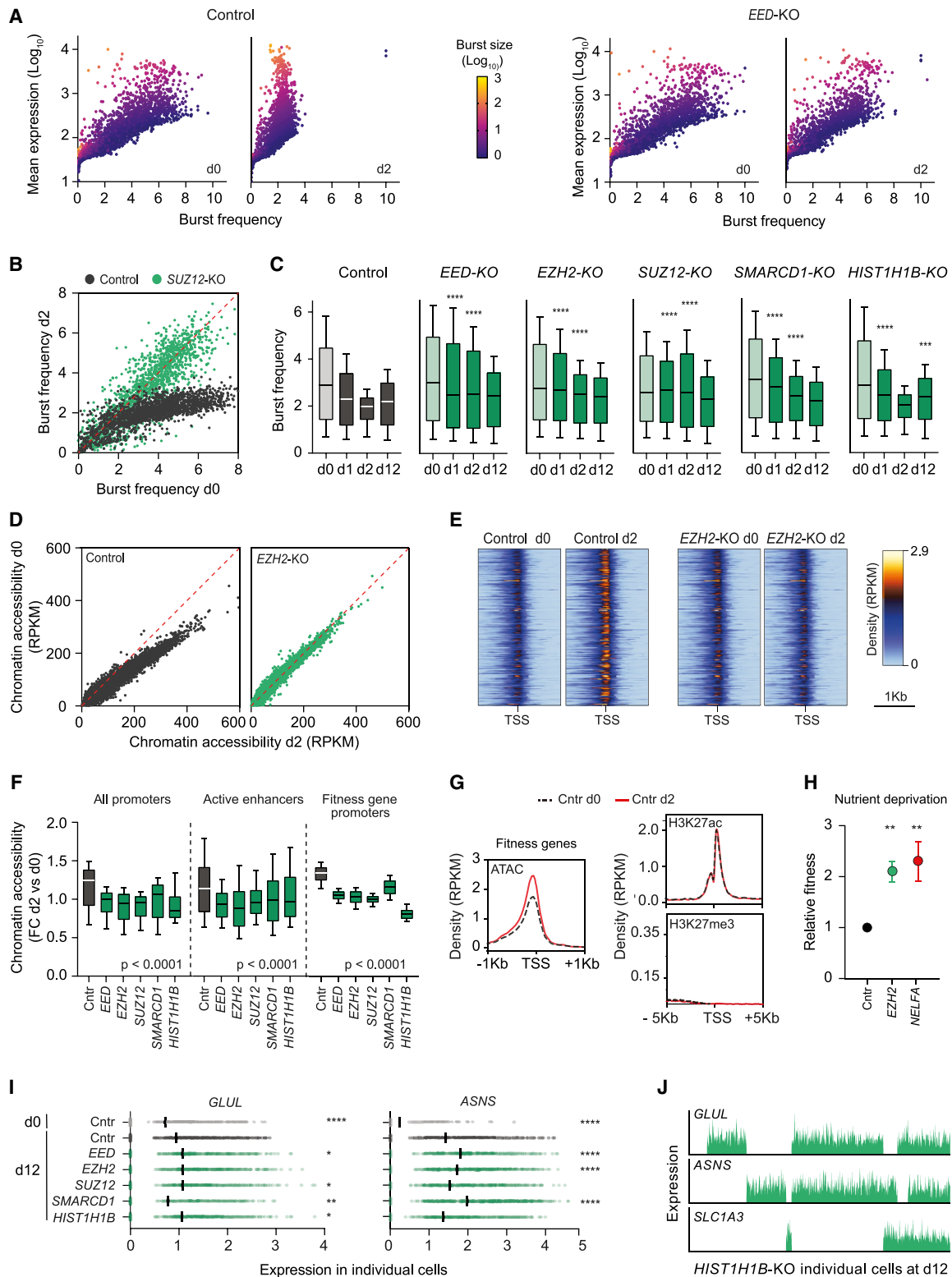
Figure 6. Transcriptional numbness of epigenetically disrupted cells

(A) Visualization of the changes in transcriptional activity induced by nutrient deprivation. Each dot is a gene.

(B) Pairwise comparison of transcriptional burst frequencies at day 0 (d0) and d2 after stress.

(C) Distributions of transcriptional burst frequencies for individual genes. ***p < 0.001 and ****p < 0.0001 relative to the same time point in control cells (two-way ANOVA, followed by Sidak's multiple comparisons). N ≥ 2,016 genes.

Since all cell populations at d12 contained a mix of stressed and resistant cells, in varying ratios, we performed clustering analysis and looked for clusters enriched for KO cells (mainly resistant subpopulations) or for control cells (mainly stressed subpopulations) (Figure 5C). Pairwise DEG analysis was then performed to identify signatures defining each subset of cells, and signatures clustered to identify common meta-signatures. The aim of this analysis was to search for possible subsets of adapted cells, i.e., displaying activation of pathways that allowed them to overcome stress. Signatures defining KO-enriched clusters were enriched for fitness signatures and depleted of stress signatures, confirming that they contained stress-resistant cells (Figure 5D). However, these cells did not show activation of pathways that could drive rewiring to an adapted state, such as reprogramming to alternative differentiation states or upregulation of compensatory metabolic pathways. Furthermore, analysis of fitness and stress genes at earlier time points revealed progressive, although mild, changes in KO cells (Figures 5E and 5F), ruling out the possibility that they had restored the initial state after reaching a fully stressed state (Figure 4Aii). In agreement with the live cell imaging analysis, these observations indicate that the stress-resistant phenotype of epigenetically disrupted cells is not due to a more efficient rewiring of cellular programs that favors cell state transitions. In fact, KO cells change less than control cells and fail to reach a fully stressed state.

The phenotypic inertia model predicts that the inability of epigenetically disrupted cells to respond to changing environments should confer tolerance to diverse types of stress as long as they impact cell fitness via transcriptional changes. Indeed, in addition to metabolic stress induced by nutrient deprivation and acidity, the selected KO populations were also resistant to thermal stress, which induces global transcriptional alterations (Aprile-Garcia et al., 2019), and buparlisib, an inhibitor of phosphatidylinositol 3-kinases (PI3Ki) that blocks cancer cell proliferation by interfering with oncogenic signaling and its downstream transcriptional effects (Maira et al., 2012) (Figure 5G).

We conclude that epigenetically disrupted cells fail to efficiently rewire gene expression programs in response to unfavorable conditions, thereby maintaining high levels of genes that support cell growth and low levels of genes that promote cell death. This blunted stress response results in enhanced tolerance to multiple types of environmental stress.

Chromatin-mediated changes in global transcriptional activity in response to stress

To uncover how inactivation of numerous and diverse epigenetic regulators converges into phenotypic inertia, we examined general features of transcriptional activity that could be broadly affected by disruption of epigenetic control. Gene transcription is discontinuous and occurs in pulses of activity interspersed by relatively long intervals of inactivity, resulting in the production of RNA molecules in discrete bursts (Tunnacliffe and Chubb, 2020). The frequency and size of transcriptional bursts can be inferred from scRNA-seq data using established methods (Larsson et al., 2019), and genome-scale profiles of burst parameters provide a readout of global transcriptional activity. We used this approach to assess (1) how environmental stress affects transcriptional activity and (2) how disruption of epigenetic control alters this response. As expected, individual genes showed a wide range of burst frequencies in unperturbed control cells, with burst intervals of few minutes for some genes and several hours for others (Larsson et al., 2019) (Figure S6A). However, the profile underwent substantial changes upon stress, with burst frequencies progressively decreasing at d1 and d2, and showing signs of recovery at d12 (Figures S6A and S6B). While the reduction affected most genes, those characterized by higher burst frequency exhibited the strongest changes (Figure S6B). We therefore examined whether high-frequency genes (HFGs; $K_{on} > 4$, Table S6) included functionally related gene sets. Strikingly, multiple fitness signatures (OXPHOS and cell-cycle-related genes, c-MYC targets, and mTOR signaling) were strongly enriched among HFGs, with false discovery rate q values up to 10^{-150} (Figure S6C). Indeed, entire sets of fitness genes showed particularly high frequencies in unperturbed cells, which strongly decreased upon stress (Figures S6D and S6E). Thus, intrinsic features of fitness genes make them particularly sensitive to the global changes in transcriptional bursting induced by stress and explain their coordinated behavior, independently of their specific regulatory networks. In line with reduced burst frequencies, fitness genes displayed up to 95% reduction in nascent RNA levels at d2 (Figure S6F), and chromatin immunoprecipitation of RNA polymerase II phosphorylated on Ser2 (p-Ser2 Pol II) confirmed inhibited transcription of fitness genes but not of stress genes (Figure S6G). Stress genes, which are low-frequency genes, did not show substantial changes in burst frequency (Figure S6H). However, their burst size progressively increased over time, likely as a result of binding of stress-activated transcription factors to their promoter (Larsson et al., 2019), showing a distinct behavior compared with all other expressed loci (Figure S6H). Thus, a normal response to stress entails a global reduction in transcriptional activity, which affects primarily high-frequency fitness genes, and upregulation of low-frequency stress genes via increased burst size. Importantly, these effects precede changes in cellular behavior.

(D) Pairwise comparison of chromatin accessibility at d0 and d2 after stress. Each dot is an ATAC-seq peak detected in merged replicates, at gene promoters or active enhancers. RPKM, reads per kilobase per million.

(E) Heatmap visualizing chromatin accessibility at the promoter of highly expressed genes (top quartile).

(F) Distributions of fold change (FC) in chromatin accessibility at individual ATAC-seq peaks detected in merged replicates. p values from one-way ANOVA followed by Dunnett's multiple comparisons. N = 70,989 (all promoters), N = 51,132 (enhancers), N = 1,056 (fitness genes) peaks.

(G) Meta-profiles of the indicated features at the promoter of fitness genes.

(H) Fitness assay under nutrient deprivation. Values are mean ± SEM from three biological replicates. **p < 0.01 (two-tailed Student's t test).

(I and J) Expression levels of the indicated genes. Lines in (I) denote median values. *p < 0.05, **p < 0.01, and ****p < 0.0001 relative to d12 control cells (Kolmogorov-Smirnov test). Each line in (J) is a cell. N ≥ 492 cells.

Whiskers of boxplots indicate the 10th and 90th percentiles, with outliers omitted for clarity. Representative graphs are shown in (A), (B), (D), (E), and (J). Other KO populations show similar patterns. See also Figures S6 and S7; Table S6.
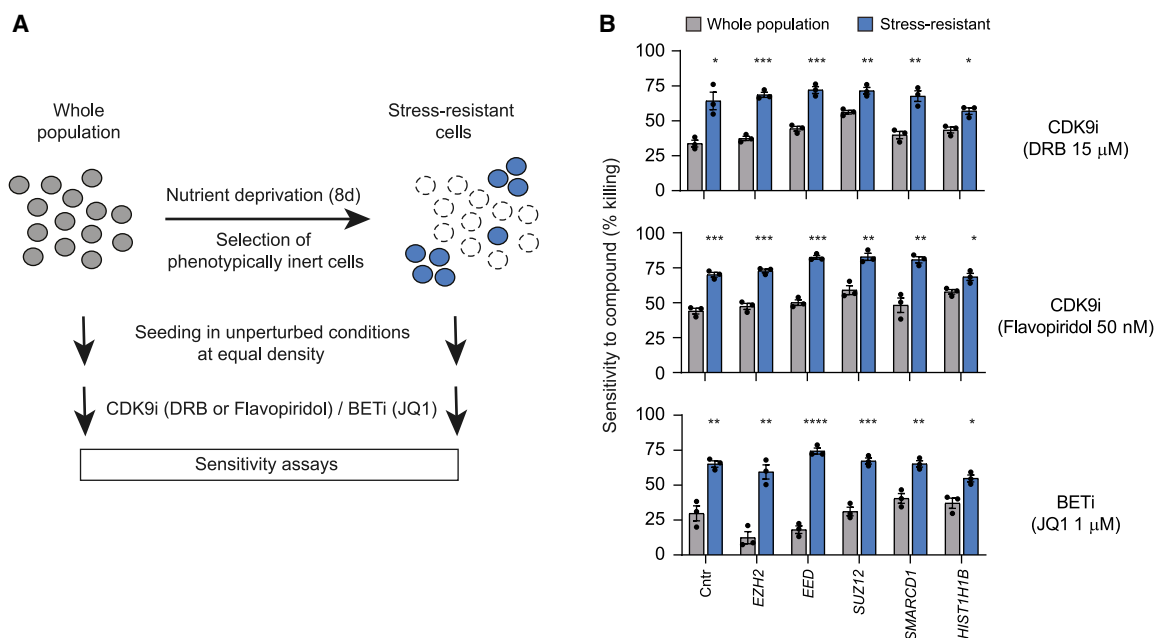
Figure 7. Hypersensitivity of stress-resistant cells to transcription inhibitors
(A) Experimental strategy used in (B).
(B) Sensitivity of the indicated cell populations to three compounds that inhibit global transcription. Values are mean ± SEM from three biological replicates.
*p < 0.05, **p < 0.01, ***p < 0.001, and ****p < 0.0001 (Student's t test).

KO populations showed distributions of burst frequency similar to those of control cells in unperturbed conditions (Figure 6A and S7A). However, the response to stress was strongly affected, and by d2 cells had only undergone mild changes (Figures 6A–6C). When compared with control cells, the distribution of burst frequency was significantly different in KO populations, with numerous HFGs, including fitness genes, retaining high frequency upon stress (Figures 6A–6C and S7A). In agreement, KO populations only showed a minor decrease in *p*-Ser2 Pol II occupancy at fitness genes, indicating that cells were unable to efficiently inhibit transcription upon stress (Figure S7B). Similarly, stress genes displayed largely unaltered patterns of burst size in the early response and only a mild increase at d12 (Figure S6H). Analysis of chromatin remodeling by assay for transposase-accessible chromatin sequencing (ATAC-seq) confirmed that KO populations were refractory to stress-induced changes. Nutrient-deprived control cells exhibited global alterations in chromatin accessibility, which disproportionately affected regions with high basal accessibility, as observed for transcriptional burst frequencies (Figures 6D–6F and S7C). Interestingly, the genome-wide reduction in burst frequencies was associated with a global increase, rather than a decrease, in chromatin accessibility and was not accompanied by substantial changes in active or repressive histone marks (Figures 6D, 6E, 6G, and S7D–S7F). These patterns resemble those associated with UV-induced transcriptional shutdown (Liakos et al., 2020) and suggest that stress-induced transcription inhibition is mediated by mechanisms distinct from canonical modalities of gene repression acting in steady-state conditions. KO populations exhibited defective chromatin remodeling, globally at promoters and enhancers, and particularly at fitness genes, which are char-

acterized by high basal levels of chromatin accessibility (Figures 6F, 6G, and S7E–S7G). Thus, the defective transcriptional response in epigenetically disrupted cells is likely due to their inability to efficiently reorganize chromatin structure across the genome in response to stress.

We finally asked whether a defective inhibition of global transcription is causal in establishing the enhanced tolerance of epigenetically disrupted cells to stress. To do so, we disrupted the negative elongation factor complex NELF, which mediates transcriptional inhibition by blocking the release of paused RNA Pol II from promoters (Aprile-Garcia et al., 2019; Rawat et al., 2021). *NELFA* KO phenocopied the effect of epigenetic disruption, conferring a fitness advantage under stress, which demonstrates that sustained transcriptional activity upon stress is sufficient to confer phenotypic inertia (Figure 6H). Altogether, these observations indicate that the inability to efficiently rewire global transcription in response to stress, a property that we name "transcriptional numbness", underpins the enhanced tolerance of epigenetically disrupted cells to unfavorable conditions.

A blunted stress response and an increased ability to survive and proliferate at early stages increase the chance for epigenetically disrupted cells to overcome a transient challenge or to find a way to cope with a sustained one. Indeed, expression of glutamine synthetase (encoded by *GLUL*), the enzyme responsible for *de novo* synthesis of glutamine (Bott et al., 2015), was detected in subsets of cells at d12 (Figure 6I). Other genes known to compensate for glutamine deficiency, such as *ASNS* (Zhang et al., 2014) and *SLC1A3* (Tajan et al., 2018), were also upregulated (Figures 6I and 6J). The expression pattern of the three genes varied within the populations, indicating that individual

cells employ various strategies for long-term survival (Figure 6J). The same genes were also detected in the few surviving control cells, suggesting that stress selects common states independently of their final abundance (Figure 6I). We conclude that phenotypic inertia in the early response to stress increases the frequency of sporadic events that promote long-term adaptation and results in a competitive advantage at the population level (see graphical abstract).

Hypersensitivity of phenotypically inert cells to CDK9 and BET inhibitors

Independently of the selective advantage it may confer, disruption of cellular homeostasis in cancer cells often creates vulnerabilities. Since a defective transcriptional rewiring underpins the observed stress-resistant phenotypes, we hypothesized that further interference with transcription may allow targeting of phenotypically inert cells. Indeed, stress-resistant cells selected after growth in nutrient-deprived conditions were hypersensitive to two CDK9 inhibitors (CDK9i) and one BET inhibitor (BETi) compared with the whole population (Figures 7A and 7B). Of note, a similar sensitivity was observed in all populations independently of the extent of stress resistance and their basal sensitivity, suggesting again that a common cellular state had been selected. Confirming the effect of the inhibitors, genetic inactivation of BRD2, BRD4, and BRD8 resulted in a rare stress-hypersensitive phenotype in large-scale fitness assay (Table S3). Since therapeutic windows exist for both classes of compounds (Bradner et al., 2017), these findings suggest a strategy to target stress-resistant cells that drive cancer evolution.

DISCUSSION

Cancer cells face many environmental challenges during tumor development, and the immediate response to these stresses dictates whether a cell will find a way to cope with it or die. Evolutionarily conserved mechanisms, including sensors of stress and effectors, orchestrate this response (Fulda et al., 2010). We show that cells deficient in a broad range of epigenetic regulators exhibit a defective transcriptional response to environmental stress, which increases their tolerance to harsh conditions and confers a competitive advantage during tumor growth. Our results provide a mechanistic explanation for the widespread selection of subclonal mutations affecting epigenetic regulators in patients (Figures 1D–1F). Phenotypic inertia of epigenetically disrupted cells has a dual beneficial effect: first, by failing to halt proliferation, stress-tolerant cells can propagate the favorable trait to their progeny and increase the size of the selectable pool; second, by raising the threshold at which individual cells suffer from stress, it delays the activation of an apoptotic program. As a combined result, the chance of long-term adaptation increases. Indeed, we find that stress-tolerant cells employ various strategies to compensate for the lack of glutamine. Notably, the same strategies are also used by rare control cells, but a higher number of stress-tolerant cells in epigenetically disrupted populations increases the frequency of these sporadic events, resulting in overall enhanced fitness at the population level. The observed tolerance to environmental stress is reminiscent of the increased tolerance to

DNA damage induced by loss of p53 (Vousden and Lu, 2002). In both cases, a faulty response to either cell-extrinsic or cell-intrinsic stress disables safeguard mechanisms that normally protect cell populations and eliminate unfit cells, thereby turning an LOF into a survival advantage.

Phenotypic inertia may extend beyond mutated epigenetic regulators and contribute to the selection of cells lacking other classes of genes involved in sensing or responding to stress. As a proof of principle, we observed enhanced fitness in cells lacking two major cellular sensors that were included in the large-scale assay as controls: the nutrient-sensing mTOR kinase and the damage-sensing ATM kinase (Table S3). Furthermore, other genes frequently inactivated across cancers, such as PTEN and FBXW7, have been linked to enhanced resistance to stress via transcription-based mechanisms (Nowak et al., 2013; Sanchez-Burgos et al., 2022).

In addition to influencing the selection of cells in the harsh microenvironment of primary tumors, phenotypic inertia may also be relevant to other aspects of tumor biology. For instance, metastatic cells in the circulation or in foreign tissues may benefit from being insensitive to surrounding conditions (Senft and Ronai, 2016). Similarly, the inability to respond to differentiation cues may help cells maintain an undifferentiated and self-renewing state (Carén et al., 2015). A defective transcriptional response may also promote resistance to targeted therapy that relies on gene expression changes, acting through a mechanism antithetic to phenotypic plasticity (Marine et al., 2020). Interestingly, both mechanisms have nongenetic bases, but while transcriptional numbness promotes the selection of an unresponsive phenotype, the ability to transition between cellular states favors adaptation through transcriptional rewiring. Notably, the enrichment of a favorable phenotype within a resistant population after weeks of growth can be explained by both scenarios. We postulate that epigenetically competent cells exploit both phenotypic plasticity and stochastic inertia, depending on the type of stress and their cellular state, while transcriptional numbness becomes dominant in epigenetically disrupted cells.

Underpinning the phenotypic inertia of epigenetically disrupted cells is their inability to efficiently remodel chromatin and decrease global transcriptional activity, which leads to a sustained expression of fitness genes that control cell proliferation and metabolism. The observation that loss of epigenetic regulators with diverse functions leads to a common defect indicates that multiple layers of epigenetic regulation are required to execute this complex transcriptional response. Several parallelisms exist between the observed effect and the transcriptional response to heat shock or UV irradiation, with seemingly unrelated stressors leading to a similar inhibition of global transcription. Interestingly, transcriptional downregulation in nutrient-deprived cells is accompanied by a genome-wide increase in chromatin accessibility, and is independent of histone modification—patterns strikingly similar to those observed upon UV irradiation (Liakos et al., 2020). Synchronous "opening" of regulatory regions across the genome may lead to RNA Pol II or other co-factors becoming limiting, affecting particularly highly expressed fitness genes that are transcribed at high frequency. More accessible promoters may also be the result of

reduced nucleosome turnover at gene bodies upon stress (Teves and Henikoff, 2011) or of an accumulation of proximally paused Pol II due to an active block of the transition to productive elongation (Aprile-Garcia et al., 2019). Future studies will be required to characterize the molecular underpinning of this noncanonical modality of gene repression and to clarify how different classes of epigenetic regulators contribute to the global chromatin reorganization induced by stress.

In conclusion, our study uncovers a mechanism through which disruption of epigenetic control confers a selective advantage to cancer cells. We propose that phenotypic inertia shapes the evolution of primary tumors harboring mutations in epigenetic regulators and, potentially, other processes that exert a selective pressure on cancer cells through environmental cues.

STAR★METHODS

Detailed methods are provided in the online version of this paper and include the following:

- ● KEY RESOURCES TABLE
- ● RESOURCE AVAILABILITY
  - ○ Lead contact
  - ○ Materials availability
  - ○ Data and code availability
- ● EXPERIMENTAL MODEL AND SUBJECT DETAILS
  - ○ Patient datasets
  - ○ Cellular models
  - ○ Mice
- ● METHOD DETAILS
  - ○ Generation of KO lines
  - ○ Large-scale fitness assays
  - ○ Validation fitness assay
  - ○ Treatment with epigenetic inhibitors
  - ○ Proliferative and apoptotic fractions
  - ○ Cell cycle analysis
  - ○ ATP assays
  - ○ Sensitivity assays
  - ○ *In vitro* competition assays
  - ○ *In vivo* competition assays
  - ○ Immunofluorescence microscopy
  - ○ Clonogenic assays
  - ○ Live-cell imaging
  - ○ RT-qPCR and nascent RNA analysis
  - ○ Chromatin immunoprecipitation (ChIP)
  - ○ Assay for transposase-accessible chromatin (ATAC)
  - ○ Exome-seq
  - ○ Bulk RNA-seq
  - ○ scRNA-seq
- ● QUANTIFICATION AND STATISTICAL ANALYSIS
  - ○ Analysis summary
  - ○ Exome-seq analysis
  - ○ Bulk RNA-seq analysis
  - ○ Gene set enrichment analysis (GSEA)
  - ○ scRNA-seq analysis
  - ○ Transcriptional burst analysis
  - ○ ATAC-seq analysis
  - ○ ChIP-seq analysis

AUTHOR CONTRIBUTIONS

I.L. and F.S. performed most of the experiments and analyzed data with help from M.M., B.T., and C.D.H.R. P.I., H.P., P.E., R.G., S.S., R.M. and W.T. performed upstream analysis of next-generation sequencing data. E.S. supervised C.D.H.R. V.S. supervised W.T. and advised on mathematical modeling. P.S. conceived and supervised the study, analyzed data, and wrote the manuscript with input from other authors.

DECLARATION OF INTERESTS

H.P. is currently an employee of Seqera Labs. E.S. is a member of the advisory board of Phenomic, consults for Theolytics and receives funding from Merck Sharp & Dohme.

INCLUSION AND DIVERSITY

We support inclusive, diverse, and equitable conduct of research.

REFERENCES

Marusyk, A., Almendro, V., and Polyak, K. (2012). Intra-tumour heterogeneity: a looking glass for cancer? Nat. Rev. Cancer *12*, 323–334. https://doi.org/10.1038/nrc3261.

Dentro, S.C., Leshchiner, I., Haase, K., Tarabichi, M., Wintersinger, J., Deshwar, A.G., Yu, K., Rubanova, Y., Macintyre, G., Demeulemeester, J., et al. (2021). Characterizing genetic intra-tumor heterogeneity across 2, 658 human cancer genomes. Cell *184*, 2239–2254.e39. https://doi.org/10.1016/j.cell.2021.03.009.

McGranahan, N., and Swanton, C. (2017). Clonal heterogeneity and tumor evolution: Past, present, and the Future. Cell *168*, 613–628. https://doi.org/10.1016/j.cell.2017.01.018.

Vendramin, R., Litchfield, K., and Swanton, C. (2021). Cancer evolution: Darwin and beyond. EMBO J. *40*, e108389. https://doi.org/10.15252/embj.2021108389.

Jamal-Hanjani, M., Wilson, G.A., McGranahan, N., Birkbak, N.J., Watkins, T.B.K., Veeriah, S., Shafi, S., Johnson, D.H., Mitter, R., Rosenthal, R., et al. (2017). Tracking the evolution of non-small-cell lung cancer. N. Engl. J. Med. *376*, 2109–2121. https://doi.org/10.1056/NEJMoa1616288.

Shen, H., and Laird, P.W. (2013). Interplay between the cancer genome and epigenome. Cell *153*, 38–55. https://doi.org/10.1016/j.cell.2013.03.008.

Lawrence, M.S., Stojanov, P., Mermel, C.H., Robinson, J.T., Garraway, L.A., Golub, T.R., Meyerson, M., Gabriel, S.B., Lander, E.S., and Getz, G. (2014).

Discovery and saturation analysis of cancer genes across 21 tumour types. Nature 505, 495–501. https://doi.org/10.1038/nature12912.

Mittal, P., and Roberts, C.W.M. (2020). The SWI/SNF complex in cancer - biology, biomarkers and therapy. Nat. Rev. Clin. Oncol. 17, 435–448. https://doi.org/10.1038/s41571-020-0357-3.

Bödör, C., Grossmann, V., Popov, N., Okosun, J., O'Riain, C., Tan, K., Marzec, J., Araf, S., Wang, J., Lee, A.M., et al. (2013). EZH2 mutations are frequent and represent an early event in follicular lymphoma. Blood 122, 3165–3168. https://doi.org/10.1182/blood-2013-04-496893.

Nikbakht, H., Panditharatna, E., Mikael, L.G., Li, R., Gayden, T., Osmond, M., Ho, C.Y., Kambhampati, M., Hwang, E.I., Faury, D., et al. (2016). Spatial and temporal homogeneity of driver mutations in diffuse intrinsic pontine glioma. Nat. Commun. 7, 11185. https://doi.org/10.1038/ncomms11185.

Turajlic, S., Xu, H., Litchfield, K., Rowan, A., Chambers, T., Lopez, J.I., Nicol, D., O'Brien, T., Larkin, J., Horswell, S., et al. (2018). Tracking cancer evolution reveals constrained Routes to Metastases: TRACERx renal. Cell 173, 581–594.e12. https://doi.org/10.1016/j.cell.2018.03.057.

Wiegand, K.C., Shah, S.P., Al-Agha, O.M., Zhao, Y., Tse, K., Zeng, T., Senz, J., McConechy, M.K., Anglesio, M.S., Kalloger, S.E., et al. (2010). ARID1A mutations in endometriosis-associated ovarian carcinomas. N. Engl. J. Med. 363, 1532–1543. https://doi.org/10.1056/NEJMoa1008433.

Martincorena, I., Fowler, J.C., Wabik, A., Lawson, A.R.J., Abascal, F., Hall, M.W.J., Cagan, A., Murai, K., Mahbubani, K., Stratton, M.R., et al. (2018). Somatic mutant clones colonize the human esophagus with age. Science 362, 911–917. https://doi.org/10.1126/science.aau3879.

Junttila, M.R., and de Sauvage, F.J. (2013). Influence of tumour micro-environment heterogeneity on therapeutic response. Nature 501, 346–354. https://doi.org/10.1038/nature12626.

Zehir, A., Benayed, R., Shah, R.H., Syed, A., Middha, S., Kim, H.R., Srinivasan, P., Gao, J., Chakravarty, D., Devlin, S.M., et al. (2017). Mutational landscape of metastatic cancer revealed from prospective clinical sequencing of 10, 000 patients. Nat. Med. 23, 703–713. https://doi.org/10.1038/nm.4333.

Robinson, D.R., Wu, Y.M., Lonigro, R.J., Vats, P., Cobain, E., Everett, J., Cao, X., Rabban, E., Kumar-Sinha, C., Raymond, V., et al. (2017). Integrative clinical genomics of metastatic cancer. Nature 548, 297–303. https://doi.org/10.1038/nature23306.

Miao, D., Margolis, C.A., Vokes, N.I., Liu, D., Taylor-Weiner, A., Wankowicz, S.M., Adeegbe, D., Keliher, D., Schilling, B., Tracy, A., et al. (2018). Genomic correlates of response to immune checkpoint blockade in microsatellite-stable solid tumors. Nat. Genet. 50, 1271–1281. https://doi.org/10.1038/s41588-018-0200-2.

Hyman, D.M., Piha-Paul, S.A., Won, H., Rodon, J., Saura, C., Shapiro, G.I., Juric, D., Quinn, D.I., Moreno, V., Doger, B., et al. (2018). HER kinase inhibition in patients with HER2- and HER3-mutant cancers. Nature 554, 189–194. https://doi.org/10.1038/nature25475.

ICGC/TCGA Pan-Cancer Analysis of Whole Genomes Consortium (2020). Pan-cancer analysis of whole genomes. Nature 578, 82–93. https://doi.org/10.1038/s41586-020-1969-6.

Nguyen, B., Fong, C., Luthra, A., Smith, S.A., DiNatale, R.G., Nandakumar, S., Walch, H., Chatila, W.K., Madupuri, R., Kundra, R., et al. (2022). Genomic characterization of metastatic patterns from prospective clinical sequencing of 25, 000 patients. Cell 185, 563–575.e11. https://doi.org/10.1016/j.cell.2022.01.003.

Gao, J., Aksoy, B.A., Dogrusoz, U., Dresdner, G., Gross, B., Sumer, S.O., Sun, Y., Jacobsen, A., Sinha, R., Larsson, E., et al. (2013). Integrative analysis of complex cancer genomics and clinical profiles using the cBioPortal. Sci. Signal. 6, pl1. https://doi.org/10.1126/scisignal.2004088.

Bitler, B.G., Aird, K.M., Garipov, A., Li, H., Amatangelo, M., Kossenkov, A.V., Schultz, D.C., Liu, Q., Shih, I.-M., Conejo-Garcia, J.R., et al. (2015). Synthetic lethality by targeting EZH2 methyltransferase activity in ARID1A-mutated cancers. Nat. Med. 21, 231–238. https://doi.org/10.1038/nm.3799.

Yokoyama, A., Somervaille, T.C.P., Smith, K.S., Rozenblatt-Rosen, O., Meyerson, M., and Cleary, M.L. (2005). The menin tumor suppressor protein is an essential oncogenic cofactor for MLL-associated leukemogenesis. Cell 123, 207–218. https://doi.org/10.1016/j.cell.2005.09.025.

Martincorena, I., Raine, K.M., Gerstung, M., Dawson, K.J., Haase, K., Van Loo, P., Davies, H., Stratton, M.R., and Campbell, P.J. (2017). Universal patterns of selection in cancer and somatic tissues. Cell 171, 1029–1041.e21. https://doi.org/10.1016/j.cell.2017.09.042.

Suzuki, H., Aoki, K., Chiba, K., Sato, Y., Shiozawa, Y., Shiraishi, Y., Shimamura, T., Niida, A., Motomura, K., Ohka, F., et al. (2015). Mutational landscape and clonal architecture in grade II and III gliomas. Nat. Genet. 47, 458–468. https://doi.org/10.1038/ng.3273.

Gerlinger, M., Horswell, S., Larkin, J., Rowan, A.J., Salm, M.P., Varela, I., Fisher, R., McGranahan, N., Matthews, N., Santos, C.R., et al. (2014). Genomic architecture and evolution of clear cell renal cell carcinomas defined by multiregion sequencing. Nat. Genet. 46, 225–233. https://doi.org/10.1038/ng.2891.

Jiang, J., Srivastava, S., and Zhang, J. (2019). Starve cancer cells of glutamine: Break the Spell or make a Hungry Monster? Cancers 11, E804. https://doi.org/10.3390/cancers11060804.

Henser-Brownhill, T., Monserrat, J., and Scaffidi, P. (2017). Generation of an arrayed CRISPR-Cas9 library targeting epigenetic regulators: from high-content screens to in vivo assays. Epigenetics 12, 1065–1075. https://doi.org/10.1080/15592294.2017.1395121.

An, O., Dall'Olio, G.M., Mourikis, T.P., and Ciccarelli, F.D. (2016). Ncg 5.0: updates of a manually curated repository of cancer genes and associated properties from cancer mutational screenings. Nucleic Acids Res. 44, D992–D999. https://doi.org/10.1093/nar/gkv1123.

Yoo, H.C., Yu, Y.C., Sung, Y., and Han, J.M. (2020). Glutamine reliance in cell metabolism. Exp. Mol. Med. 52, 1496–1516. https://doi.org/10.1038/s12276-020-00504-8.

Laugesen, A., Høifeldt, J.W., and Helin, K. (2016). Role of the Polycomb repressive complex 2 (PRC2) in transcriptional regulation and cancer. Cold Spring Harb. Perspect. Med. 6, a026575. https://doi.org/10.1101/cshperspect.a026575.

Ferrara, N. (2005). VEGF as a therapeutic target in cancer. Oncology 69 (Suppl 3), 11–16. https://doi.org/10.1159/000088479.

Sabatini, D.M. (2017). Twenty-five years of mTOR: Uncovering the link from nutrients to growth. Proc. Natl. Acad. Sci. USA 114, 11818–11825. https://doi.org/10.1073/pnas.1716173114.

Carlson, M., and Laurent, B.C. (1994). The SNF/SWI family of global transcriptional activators. Curr. Opin. Cell Biol. 6, 396–402. https://doi.org/10.1016/0955-0674(94)90032-9.

Scaffidi, P. (2016). Histone H1 alterations in cancer. Biochim. Biophys. Acta 1859, 533–539. https://doi.org/10.1016/j.bbagrm.2015.09.008.

Kondo, H., Ratcliffe, C.D.H., Hooper, S., Ellis, J., MacRae, J.I., Hennequart, M., Dunsby, C.W., Anderson, K.I., and Sahai, E. (2021). Single-cell resolved imaging reveals intra-tumor heterogeneity in glycolysis, transitions between metabolic states, and their regulatory mechanisms. Cell Rep. 34, 108750. https://doi.org/10.1016/j.celrep.2021.108750.

Aprile-Garcia, F., Tomar, P., Hummel, B., Khavaran, A., and Sawarkar, R. (2019). Nascent-protein ubiquitination is required for heat shock-induced gene downregulation in human cells. Nat. Struct. Mol. Biol. 26, 137–146. https://doi.org/10.1038/s41594-018-0182-x.

Maira, S.M., Pecchi, S., Huang, A., Burger, M., Knapp, M., Sterker, D., Schnell, C., Guthy, D., Nagel, T., Wiesmann, M., et al. (2012). Identification and characterization of NVP-BKM120, an orally available pan-class I PI3-kinase inhibitor. Mol. Cancer Ther. 11, 317–328. https://doi.org/10.1158/1535-7163.Mct-11-0474.

Tunnacliffe, E., and Chubb, J.R. (2020). What is a transcriptional burst? Trends Genet. 36, 288–297. https://doi.org/10.1016/j.tig.2020.01.003.

Larsson, A.J.M., Johnsson, P., Hagemann-Jensen, M., Hartmanis, L., Faridani, O.R., Reinius, B., Segerstolpe, Å., Rivera, C.M., Ren, B., and Sandberg, R. (2019). Genomic encoding of transcriptional burst kinetics. Nature 565, 251–254. https://doi.org/10.1038/s41586-018-0836-1.

Liakos, A., Konstantopoulos, D., Lavigne, M.D., and Fousteri, M. (2020). Continuous transcription initiation guarantees robust repair of all transcribed genes and regulatory regions. Nat. Commun. *11*, 916. https://doi.org/10.1038/s41467-020-14566-9.

Rawat, P., Boehning, M., Hummel, B., Aprile-Garcia, F., Pandit, A.S., Eisenhardt, N., Khavaran, A., Niskanen, E., Vos, S.M., Palvimo, J.J., et al. (2021). Stress-induced nuclear condensation of NELF drives transcriptional downregulation. Mol. Cell *81*, 1013–1026.e11. https://doi.org/10.1016/j.molcel.2021.01.016.

Bott, A.J., Peng, I.C., Fan, Y., Faubert, B., Zhao, L., Li, J., Neidler, S., Sun, Y., Jaber, N., Krokowski, D., et al. (2015). Oncogenic Myc induces expression of glutamine synthetase through promoter Demethylation. Cell Metab. *22*, 1068–1077. https://doi.org/10.1016/j.cmet.2015.09.025.

Zhang, J., Fan, J., Venneti, S., Cross, J.R., Takagi, T., Bhinder, B., Djaballah, H., Kanai, M., Cheng, E.H., Judkins, A.R., et al. (2014). Asparagine plays a critical role in regulating cellular adaptation to glutamine depletion. Mol. Cell *56*, 205–218. https://doi.org/10.1016/j.molcel.2014.08.018.

Tajan, M., Hock, A.K., Blagih, J., Robertson, N.A., Labuschagne, C.F., Kruiswijk, F., Humpton, T.J., Adams, P.D., and Vousden, K.H. (2018). A role for p53 in the adaptation to glutamine Starvation through the expression of SLC1A3. Cell Metab. *28*, 721–736.e6. https://doi.org/10.1016/j.cmet.2018.07.005.

Bradner, J.E., Hnisz, D., and Young, R.A. (2017). Transcriptional Addiction in cancer. Cell *168*, 629–643. https://doi.org/10.1016/j.cell.2016.12.013.

Fulda, S., Gorman, A.M., Hori, O., and Samali, A. (2010). Cellular stress responses: cell survival and cell death. Int. J. Cell Biol. *2010*, 214074. https://doi.org/10.1155/2010/214074.

Vousden, K.H., and Lu, X. (2002). Live or let die: the cell's response to p53. Nat. Rev. Cancer *2*, 594–604. https://doi.org/10.1038/nrc864.

Nowak, K., Seisenbacher, G., Hafen, E., and Stocker, H. (2013). Nutrient restriction enhances the proliferative potential of cells lacking the tumor suppressor PTEN in mitotic tissues. eLife *2*, e00380. https://doi.org/10.7554/eLife.00380.

Sanchez-Burgos, L., Navarro-González, B., García-Martín, S., Sirozh, O., Mota-Pino, J., Fueyo-Marcos, E., Tejero, H., Antón, M.E., Murga, M., Al-Shahrour, F., and Fernandez-Capetillo, O. (2022). Activation of the integrated stress response is a vulnerability for multidrug-resistant FBXW7-deficient cells. EMBO Mol. Med. e15855. https://doi.org/10.15252/emmm.202215855.

Senft, D., and Ronai, Z.A. (2016). Adaptive stress responses during tumor Metastasis and Dormancy. Trends Cancer *2*, 429–442. https://doi.org/10.1016/j.trecan.2016.06.004.

Carén, H., Stricker, S.H., Bulstrode, H., Gagrica, S., Johnstone, E., Bartlett, T.E., Feber, A., Wilson, G., Teschendorff, A.E., Bertone, P., et al. (2015). Glioblastoma Stem cells respond to differentiation cues but fail to Undergo Commitment and Terminal cell-cycle arrest. Stem Cell Rep. *5*, 829–842. https://doi.org/10.1016/j.stemcr.2015.09.014.

Marine, J.-C., Dawson, S.-J., and Dawson, M.A. (2020). Non-genetic mechanisms of therapeutic resistance in cancer. Nat. Rev. Cancer *20*, 743–756. https://doi.org/10.1038/s41568-020-00302-4.

Teves, S.S., and Henikoff, S. (2011). Heat shock reduces stalled RNA polymerase II and nucleosome turnover genome-wide. Genes Dev. *25*, 2387–2397. https://doi.org/10.1101/gad.177675.111.

Vogelstein, B., Papadopoulos, N., Velculescu, V.E., Zhou, S., Diaz, L.A., Jr., and Kinzler, K.W. (2013). Cancer genome landscapes. Science *339*, 1546–1558. https://doi.org/10.1126/science.1235122.

Monserrat, J., Morales Torres, C., Richardson, L., Wilson, T.S., Patel, H., Domart, M.C., Horswell, S., Song, O.R., Jiang, M., Crawford, M., et al. (2021). Disruption of the MSL complex inhibits tumour maintenance by exacerbating chromosomal instability. Nat. Cell Biol. *23*, 401–412. https://doi.org/10.1038/s41556-021-00657-2.

Cen, H., Mao, F., Aronchik, I., Fuentes, R.J., and Firestone, G.L. (2008). DEVD-NucView488: a novel class of enzyme substrates for real-time detection of caspase-3 activity in live cells. FASEB J. Off. Publ. Fed. Am. Soc. Exp. Biol. *22*, 2243–2252. https://doi.org/10.1096/fj.07-099234.

Raab, M., Gentili, M., de Belly, H., Thiam, H.R., Vargas, P., Jimenez, A.J., Lautenschlaeger, F., Voituriez, R., Lennon-Duménil, A.M., Manel, N., and Piel, M. (2016). ESCRT III repairs nuclear envelope ruptures during cell migration to limit DNA damage and cell death. Science *352*, 359–362. https://doi.org/10.1126/science.aad7611.

Zhang, W., Lohman, A.W., Zhuravlova, Y., Lu, X., Wiens, M.D., Hoi, H., Yaganoglu, S., Mohr, M.A., Kitova, E.N., Klassen, J.S., et al. (2017). Optogenetic control with a photocleavable protein. Nat. Methods *14*, 391–394. https://doi.org/10.1038/nmeth.4222.

Morales Torres, C., Wu, M.Y., Hobor, S., Wainwright, E.N., Martin, M.J., Patel, H., Grey, W., Grönroos, E., Howell, S., Carvalho, J., et al. (2020). Selective inhibition of cancer cell self-renewal through a Quisinostat-histone H1.0 axis. Nat. Commun. *11*, 1792. https://doi.org/10.1038/s41467-020-15615-z.

Li, H., and Durbin, R. (2009). Fast and accurate short read alignment with Burrows-Wheeler transform. Bioinformatics *25*, 1754–1760. https://doi.org/10.1093/bioinformatics/btp324.

Bankhead, P., Loughrey, M.B., Fernández, J.A., Dombrowski, Y., McArt, D.G., Dunne, P.D., McQuaid, S., Gray, R.T., Murray, L.J., Coleman, H.G., et al. (2017). QuPath: Open source software for digital pathology image analysis. Sci. Rep. *7*, 16878. https://doi.org/10.1038/s41598-017-17204-5.

Liang, Q., Kong, J., Stalker, J., and Bradley, A. (2009). Chromosomal mobilization and reintegration of Sleeping Beauty and PiggyBac transposons. Genesis *47*, 404–408. https://doi.org/10.1002/dvg.20508.

Simeoni, F., Romero-Camarero, I., Camera, F., Amaral, F.M.R., Sinclair, O.J., Papachristou, E.K., Spencer, G.J., Lie-A-Ling, M., Lacaud, G., Wiseman, D.H., et al. (2021). Enhancer recruitment of transcription repressors RUNX1 and TLE3 by mis-expressed FOXC1 blocks differentiation in acute myeloid leukemia. Cell Rep. *36*, 109725. https://doi.org/10.1016/j.celrep.2021.109725.

Corces, M.R., Trevino, A.E., Hamilton, E.G., Greenside, P.G., Sinnott-Armstrong, N.A., Vesuna, S., Satpathy, A.T., Rubin, A.J., Montine, K.S., Wu, B., et al. (2017). An improved ATAC-seq protocol reduces background and enables interrogation of frozen tissues. Nat. Methods *14*, 959–962. https://doi.org/10.1038/nmeth.4396.

Hennig, B.P., Velten, L., Racke, I., Tu, C.S., Thoms, M., Rybin, V., Besir, H., Remans, K., and Steinmetz, L.M. (2018). Large-scale low-Cost NGS library preparation using a robust Tn5 Purification and Tagmentation protocol. G3 (Bethesda) *8*, 79–89. https://doi.org/10.1534/g3.117.300257.

Vasimuddin, M., Misra, S., Li, H., and Aluru, S. (2019). Efficient Architecture-Aware Acceleration of BWA-MEM for Multicore Systems, pp. 314–324.

Van der Auwera, G.A., Carneiro, M.O., Hartl, C., Poplin, R., del Angel, G., Levy-Moonshine, A., Jordan, T., Shakir, K., Roazen, D., Thibault, J., et al. (2013). From FastQ data to high-confidence variant calls: the genome analysis Toolkit best Practices pipeline. Curr. Protoc. Bioinf. *43*, 11.10.1–11.10.33. https://doi.org/10.1002/0471250953.bi1110s43.

Saunders, C.T., Wong, W.S.W., Swamy, S., Becq, J., Murray, L.J., and Cheetham, R.K. (2012). Strelka: accurate somatic small-variant calling from sequenced tumor-normal sample pairs. Bioinformatics *28*, 1811–1817. https://doi.org/10.1093/bioinformatics/bts271.

Cingolani, P., Platts, A., Wang, L.L., Coon, M., Nguyen, T., Wang, L., Land, S.J., Lu, X., and Ruden, D.M. (2012). A program for annotating and predicting the effects of single nucleotide polymorphisms, SnpEff: SNPs in the genome of Drosophila melanogaster strain w1118; iso-2; iso-3. Fly *6*, 80–92. https://doi.org/10.4161/fly.19695.

Garcia, M., Juhos, S., Larsson, M., Olason, P.I., Martin, M., Eisfeldt, J., DiLorenzo, S., Sandgren, J., Díaz De Ståhl, T., Ewels, P., et al. (2020). Sarek: a portable workflow for whole-genome sequencing analysis of germline and somatic variants. F1000Res. *9*, 63. https://doi.org/10.12688/f1000research.16665.2.

Ewels, P.A., Peltzer, A., Fillinger, S., Patel, H., Alneberg, J., Wilm, A., Garcia, M.U., Di Tommaso, P., and Nahnsen, S. (2020). The nf-core framework for community-curated bioinformatics pipelines. Nat. Biotechnol. *38*, 276–278. https://doi.org/10.1038/s41587-020-0439-x.

Di Tommaso, P., Chatzou, M., Floden, E.W., Barja, P.P., Palumbo, E., and Notredame, C. (2017). Nextflow enables reproducible computational workflows. Nat. Biotechnol. *35*, 316–319. https://doi.org/10.1038/nbt.3820.

Martin, M. (2011). Cutadapt removes adapter sequences from high-throughput sequencing reads. EMBnet. j. *17*, 10–12.

Li, B., and Dewey, C.N. (2011). RSEM: accurate transcript quantification from RNA-Seq data with or without a reference genome. BMC Bioinf. *12*, 323. https://doi.org/10.1186/1471-2105-12-323.

Dobin, A., Davis, C.A., Schlesinger, F., Drenkow, J., Zaleski, C., Jha, S., Batut, P., Chaisson, M., and Gingeras, T.R. (2013). STAR: ultrafast universal RNA-seq aligner. Bioinformatics *29*, 15–21. https://doi.org/10.1093/bioinformatics/bts635.

Karolchik, D., Hinrichs, A.S., Furey, T.S., Roskin, K.M., Sugnet, C.W., Haussler, D., and Kent, W.J. (2004). The UCSC Table Browser data retrieval tool. Nucleic Acids Res. *32*, D493–D496. https://doi.org/10.1093/nar/gkh103.

Love, M.I., Huber, W., and Anders, S. (2014). Moderated estimation of fold change and dispersion for RNA-seq data with DESeq2. Genome Biol. *15*, 550. https://doi.org/10.1186/s13059-014-0550-8.

Team, R.C. (2015). R: A Language and Environment for Statistical Computing (R Foundation for Statistical Computing). http://www.R-project.org/.

Subramanian, A., Tamayo, P., Mootha, V.K., Mukherjee, S., Ebert, B.L., Gillette, M.A., Paulovich, A., Pomeroy, S.L., Golub, T.R., Lander, E.S., and Mesirov, J.P. (2005). Gene set enrichment analysis: a knowledge-based approach for interpreting genome-wide expression profiles. Proc. Natl. Acad. Sci. USA *102*, 15545–15550. https://doi.org/10.1073/pnas.0506580102.

Kuhn, M. (2008). Building Predictive Models in R Using the Caret Package, *28*, p. 26. https://doi.org/10.18637/jss.v028.i05.

McCarthy, D.J., Campbell, K.R., Lun, A.T.L., and Wills, Q.F. (2017). Scater: pre-processing, quality control, normalization and visualization of single-cell RNA-seq data in R. Bioinformatics *33*, 1179–1186. https://doi.org/10.1093/bioinformatics/btw777.

Ilicic, T., Kim, J.K., Kolodziejczyk, A.A., Bagger, F.O., McCarthy, D.J., Marioni, J.C., and Teichmann, S.A. (2016). Classification of low quality cells from single-cell RNA-seq data. Genome Biol. *17*, 29. https://doi.org/10.1186/s13059-016-0888-1.

Lun, A.T.L., McCarthy, D.J., and Marioni, J.C. (2016). A step-by-step workflow for low-level analysis of single-cell RNA-seq data with Bioconductor. F1000Res. *5*, 2122. https://doi.org/10.12688/f1000research.9501.2.

Stuart, T., Butler, A., Hoffman, P., Hafemeister, C., Papalexi, E., Mauck, W.M., 3rd, Hao, Y., Stoeckius, M., Smibert, P., and Satija, R. (2019). Comprehensive integration of single-cell data. Cell *177*, 1888–1902.e21. https://doi.org/10.1016/j.cell.2019.05.031.

Ahlmann-Eltze, C., and Huber, W. (2021). glmGamPoi: fitting Gamma-Poisson generalized linear models on single cell count data. Bioinformatics *36*, 5701–5702. https://doi.org/10.1093/bioinformatics/btaa1009.

Brennecke, P., Anders, S., Kim, J.K., Kołodziejczyk, A.A., Zhang, X., Proserpio, V., Baying, B., Benes, V., Teichmann, S.A., Marioni, J.C., and Heisler, M.G. (2013). Accounting for technical noise in single-cell RNA-seq experiments. Nat. Methods *10*, 1093–1095. https://doi.org/10.1038/nmeth.2645.

Jarvis, R.A., and Patrick, E.A. (1973). Clustering using a similarity measure based on shared near neighbors. IEEE Transactions on Computers. IEEE Trans. Comput. *C-22*, 1025–1034. https://doi.org/10.1109/T-C.1973.223640.

Monti, S., Tamayo, P., Mesirov, J., and Golub, T. (2003). Consensus clustering: a Resampling-based method for class Discovery and visualization of gene expression Microarray data. Mach. Learn. *52*, 91–118. https://doi.org/10.1023/A:1023949509487.

Finak, G., McDavid, A., Yajima, M., Deng, J., Gersuk, V., Shalek, A.K., Slichter, C.K., Miller, H.W., McElrath, M.J., Prlic, M., et al. (2015). MAST: a flexible statistical framework for assessing transcriptional changes and characterizing heterogeneity in single-cell RNA sequencing data. Genome Biol. *16*, 278. https://doi.org/10.1186/s13059-015-0844-5.

Sokal, R.R., and Rohlf, F.J. (1962). The comparison of dendrograms by objective methods. Taxon *11*, 33–40. https://doi.org/10.2307/1217208.

Rousseeuw, P.J. (1987). Silhouettes: a graphical aid to the interpretation and validation of cluster analysis. J. Comput. Appl. Math. *20*, 53–65. https://doi.org/10.1016/0377-0427(87)90125-7.

Peccoud, J., and Ycart, B. (1995). Markovian modeling of gene-product synthesis. Theor. Popul. Biol. *48*, 222–234.

Patel, H., Ewels, P., Espinosa-Carrasco, J., Peltzer, A., Behrens, D., Gabernet, G., Jin, M., Hörtenhuber, M., and Garcia, M.U. (2022). Nf-Core/Atacseq: Nf-Core/atacseq v1.2.2 - Iron Ossifrage (1.2.2) (Zenodo). https://doi.org/10.5281/zenodo.6544493.

Ramírez, F., Ryan, D.P., Grüning, B., Bhardwaj, V., Kilpert, F., Richter, A.S., Heyne, S., Dündar, F., and Manke, T. (2016). deepTools2: a next generation web server for deep-sequencing data analysis. Nucleic Acids Res. *44*, W160–W165. https://doi.org/10.1093/nar/gkw257.

Patel, H., Wang, C., Ewels, P., Chedraoui Silva, T., Peltzer, A., Behrens, D., Garcia, M., Rotholandus, M., Haglund, S., and Kretzschmar, W. (2021). Nf-Core/Chipseq: Nf-Core/chipseq v1.2.2 - Rusty Mole (1.2.2) (Zenodo). https://doi.org/10.5281/zenodo.4711243.

STAR★METHODS

KEY RESOURCES TABLE

REAGENT or RESOURCE	SOURCE	IDENTIFIER
Antibodies		
Mouse monoclonal anti-Lamin A/C (636)	Santa Cruz Biotechnology	Cat#sc-7292; RRID:AB_627875
Rabbit polyclonal anti-trimethyl-Histone H3 (Lys27)	EMD Millipore	Cat#07-449; RRID:AB_310624
Rabbit polyclonal anti-acetyl-Histone H4 (Lys16)	Cell Signaling Technology	Cat#2591
Rabbit polyclonal anti-phospho-S6 Ribosomal Protein (Ser235/236)	Cell Signaling Technology	Cat#2211; RRID:AB_331679
Rabbit monoclonal anti-RNA polymerase II CTD repeat YSPTSPS (phospho S2) antibody [EPR18855-87]	Abcam	Cat#ab238146-100ul; RRID: AB_2905557
Donkey anti-Rabbit IgG (H + L) Highly Cross-Adsorbed Secondary Antibody, Alexa Fluor™ 488	ThermoFisher Scientific	Cat#A10042; RRID:AB_2535792
Donkey anti-Rabbit IgG (H + L) Highly Cross-Adsorbed Secondary Antibody, Alexa Fluor™ 568	ThermoFisher Scientific	Cat#A-21206; RRID:AB_2534017
Rabbit monoclonal anti-trimethyl-Histone H3 (Lys27) (C36B11)	Cell Signaling Technology	Cat#9733; RRID:AB_2616029
Rabbit monoclonal anti-acetyl-Histone H3 (Lys27) (D5E4)	Cell Signaling Technology	Cat#8173; RRID: AB_10949503
Rabbit polyclonal anti-monomethyl-Histone H3 (Lys4)	Abcam	Cat#ab8895; RRID: AB_306847
Rabbit polyclonal anti-trimethyl-Histone H3 (Lys4)	Abcam	Cat# ab8580; RRID: AB_306649
Bacterial and virus strains		
N/A	N/A	N/A
Biological samples		
Patient Derived Xenograft MEFX 2090	Charles Rivers tumor model compendium	https://compendium.criver.com/
Patient Derived Xenograft LXFL 1674	Charles Rivers tumor model compendium	https://compendium.criver.com/
Patient Derived Xenograft PAXF 1997	Charles Rivers tumor model compendium	https://compendium.criver.com/
Patient Derived Xenograft BXF 1352	Charles Rivers tumor model compendium	https://compendium.criver.com/
Patient Derived Xenograft CXF 269	Charles Rivers tumor model compendium	https://compendium.criver.com/
Pan-cancer cohorts (Mutational data)	Campbell, 2020; Hyman et al., 2018; Miao et al., 2018; Nguyen et al., 2022; Robinson et al., 2017; Zehir et al., 2017	https://www.cbioportal.org/
TRACERx cohort (Mutational data)	Jamal-Hanjani et al., 2017	N/A
LGG cohort (Mutational data)	Suzuki et al., 2015	N/A
Chemicals, peptides, and recombinant proteins		
FuGENE® HD Transfection Reagent	Promega	Cat#E2311
5× siRNA Buffer	Horizon	Cat#B-002000-UB-100
DharmaFECT™ Duo Transfection Reagent	Horizon	Cat#T-2010-01

(Continued on next page)

Continued

REAGENT or RESOURCE	SOURCE	IDENTIFIER
Paraformaldehyde, 16% w/v aq. soln., methanol free	Alfa Aesar	Cat#43368
SYTOX™ Green Nucleic Acid Stain	ThermoFisher Scientific	Cat#S7020
SYTOX™ Deep Red Nucleic Acid Stain	ThermoFisher Scientific	Cat#S11380
Hydroxyurea	Sigma-Aldrich	Cat#H8627
Proteinase K	Qiagen	Cat#19131
RGFP966	APExBIO	Cat#A8803
Tubastatin A	APExBIO	Cat#A4101
EX 527 (SEN0014196)	APExBIO	Cat#A4181
EPZ004777	APExBIO	Cat#A4170
MM-102	APExBIO	Cat#B1582
WM-8014	APExBIO	Cat#A8779
GSK126	Stratech	Cat#S7061-SEL
Quisinostat	Insight Biotechnology	Cat#HY-15433
JIB-04	APExBIO	Cat#B1579
Buparlisib	Generon	Cat#HY-70063
5,6-Dichlorobenzimidazole 1-β-D-ribofuranoside	Merck Life Science UK	Cat#D1916
Flavopiridol hydrochloride hydrate	Merck Life Science UK	Cat#F3055
(+)-JQ1	Merck Life Science UK	Cat#SML1524
Ac-DEVD-NucView488	The Francis Crick Institute	Cen et al., 2008
Tetramethylrhodamine ethyl ester perchlorate (TMRE)	ThermoFisher Scientific	Cat#T669
Bevacizumab (anti-VEGF recombinant antibody)	Stratech	Cat#A2006-SEL-5mg
Dynabeads (Protein G)	ThermoFisher Scientific	Cat#10003D
AMPure XP Reagent	Beckman Coulter	Cat# A63881
Sulfo-Cyanine5 azide	Lumiprobe	Cat# A3330
Critical commercial assays		
Click-iT™ EdU Cell Proliferation Kit	ThermoFisher Scientific	Cat#C10340
Dneasy Blood & Tissue kit	Qiagen	Cat#69506
QIAquick PCR Purification Kit	Qiagen	Cat#28104
QIAquick Gel Extraction kit	Qiagen	Cat#28706
Rneasy Plus Micro Kit	Qiagen	Cat#74034
Herculase II Fusion Enzyme Kit	Agilent Technologies	Cat#600679
High Capacity cDNA Reverse Transcription Kit	ThermoFisher Scientific	Cat#4368814
SsoAdvanced™ Universal SYBR® Green Supermix	Bio-Rad	Cat#172-5274
MiSeq Reagent Nano Kit V2	Illumina	Cat#MS-102-2001
TURBO DNase	ThermoFisher Scientific	Cat#AM2238
QuantiFluor dsDNA system	Promega	Cat#E2670
Genomic DNA ScreenTape	Agilent Technologies	Cat#5067-5365
Genomic DNA Reagents	Agilent Technologies	Cat#5067-5366
NEBNext Ultra II DNA library prep kit for Illumina	NEB	Cat#E7645S
NEBNext® Multiplex Oligos for Illumina® (96 Unique Dual Index Primer Pairs)	NEB	Cat#E6440S
NEBNext® High-Fidelity 2X PCR Master Mix	NEB	Cat# M0541S

Continued

REAGENT or RESOURCE	SOURCE	IDENTIFIER
Twist Human Core Exome kit	Twist Bioscience	Cat#100578; Cat#101174; Cat#100254
QuantiFluor RNA system	Promega	Cat#E3310
High Sensitivity RNA ScreenTape	Agilent Technologies	Cat#5067-5579
QuantSeq 3′ mRNA-Seq Library Prep Kit FWD for Illumina	Lexogen	Cat#015
Chromium Single Cell 3′ Reagent Kits v3.1	10x Genomics	Cat#CG000205
CellTiter-Glo® 2.0 Cell Viability Assay	Promega	Cat#G9242
DNA Clean & Concentrator	Zymo research	Cat#D4004
Tn5 transposase	Crick Structural Biology STP	N/A
Deposited data		
Exome-seq	This paper; NCBI Gene Expression Omnibus	GEO: GSE178643, GSE178642
Bulk RNA-seq	This paper; NCBI Gene Expression Omnibus	GEO: GSE178643, GSE178306
Single-cell RNA-seq	This paper; NCBI Gene Expression Omnibus	GEO: GSE178643, GSE178641
ATAC-seq	This paper; NCBI Gene Expression Omnibus	GEO: GSE178643, GSE212744
ChIP-seq	This paper; NCBI Gene Expression Omnibus	GEO: GSE178643, GSE212693
Z score from large-scale fitness assays	This paper	Table S3
Experimental models: Cell lines		
PDX MEFX 2090 derived cells	This paper	Table S2
PDX LXFL 1674 derived cells	This paper	Table S2
PDX PAXF 1997 derived cells	This paper	Table S2
PDX BXF 1352 derived cells	This paper	Table S2
PDX CXF 269 derived cells	This paper	Table S2
PDX MEFX 2090 GFP NLS	This paper	N/A
PDX MEFX 2090 MCHERRY NLS	This paper	N/A
PDX MEFX 2090 GLUCOSE FRET SENSOR	This paper	N/A
HEK293T	Francis Crick Institute cell line repository	N/A
Experimental models: Organisms/strains		
NSG mice (NOD.Cg-Prkdc^{scid}Il2rg^{tm1Wjl}/SzJ)	Francis Crick Institute colony	N/A
Oligonucleotides		
Primers used in qPCR assays for total and nascent mRNA levels	This paper	Table S7
Primers used in ChIP-qPCR assays	This paper	Table S7
Primers used for cloning	This paper	Table S7
Primers used for library preparation and NGS for the *in vivo* competition experiment	This paper	Table S7
Synthetic construct carrying an engineered sgRNA scaffold with a 3′ terminal Capture Sequence 1 and is compatible with the 10x Genomics Feature barcoding technology	This paper	Table S7

Continued

REAGENT or RESOURCE	SOURCE	IDENTIFIER
sgRNA sequences in the engineered pLenti-BSD-sgRNA plasmid used for 10x Gemonics scRNAseq with Feature Barcoding Technology for CRISPR screening	This paper	Table S7
Synthetic crRNAs used to generate KO cells	This paper	Table S7
Recombinant DNA		
Plasmid: pCW-Cas9	Monserrat et al., 2021	N/A
Plasmid: psPax2	Trono Lab	Addgene; Cat#12260; RRID:Addgene_12260
Plasmid: pMD2.G	Trono Lab	Addgene; Cat#12259; RRID:Addgene_12259
Plasmid: pAdVAntage™ Vector	Promega	Cat#E1711
Plasmid: arrayed lentiviral sgRNA library	Henser-Brownhill et al., 2017	N/A
Plasmid: pTRIP-SFFV-EGFP-NLS	Raab et al., 2016	Addgene; Cat#86677; RRID:Addgene_86677
Plasmid: pUAS-mCherry-NLS	Zhang et al., 2017	Addgene; Cat#87695; RRID:Addgene_87695
Plasmid: pTRIP-SFFV-mCherry-NLS	This paper	N/A
Plasmid: PiggyBac transposon carrying FRET biosensor	Kondo et al., 2021	N/A
Plasmid: PB transposase (PBase)	Liang et al., 2009	N/A
Plasmid: pLenti-BSD-sgRNA-Capture_seq_1E	This paper	Table S7
Software and algorithms		
ImageJ 1.45s	NIH	RRID:SCR_003070; https://imagej.nih.gov/ij/
QuPath-0.2.2	Bankhead, P. et al., 2017	RRID:SCR_018257; https://qupath.github.io
Zeiss Zen software (v2.3)	ZEISS	N/A
Incucyte® S3 Live-Cell Analysis System	Sartorius	RRID:SCR_019874; https://www.sartorius.com/en/products/live-cell-imaging-analysis/live-cell-analysis-instruments
Gene Set Enrichment Analysis (GSEA)	GSEA (Broad Institute)	RRID:SCR_003199; http://www.broadinstitute.org/gsea/
Prism 9	GraphPad Software	RRID:SCR_002798; https://www.graphpad.com/
CellRanger (v3.0.2)	10x Genomics	RRID:SCR_017344; https://support.10xgenomics.com/single-cell-gene-expression/software/pipelines/latest/what-is-cell-ranger
FASTX-Toolkit	N/A	RRID:SCR_005534; http://hannonlab.cshl.edu/fastx_toolkit
BWA (v0.5.9-r16)	Li and Durbin, 2009	RRID:SCR_010910; https://github.com/lh3/bwa
Trim Galore (v0.6.4_dev)	Felix Krueger	RRID:SCR_011847; https://www.bioinformatics.babraham.ac.uk/projects/trim_galore/
GATK MarkDuplicatesSpark (v4.1.7.0)	Van der Auwera et al., 2013	https://github.com/broadinstitute/gatk
ApplyBQSR (GATK v4.1.7.0)	N/A	https://github.com/broadinstitute/gatk
Strelka2 (v2.9.10)	Saunders et al., 2012	https://github.com/Illumina/strelka/releases
SnpEff (v4.3t, SnpEff DB version GRCh38.86)	Cingolani et al., 2012	RRID:SCR_005191; https://github.com/pcingola/SnpEff

(Continued on next page)

Continued

REAGENT or RESOURCE	SOURCE	IDENTIFIER
nf-core/chipseq (v1.2.2)	Patel et al., 2021	https://github.com/nf-core/chipseq
nf-core/atacseq (v1.2.2)	Patel et al., 2022	https://github.com/nf-core/atacseq
nfcore/sarek pipeline (v2.6.1)	Ewels et al., 2020; Garcia et al., 2020	https://github.com/nf-core/sarek
Nextflow (v20.11.0-edge)	Di Tommaso et al., 2017	https://github.com/nextflow-io/nextflow
deepTools (v2.0)	Ramirez et al., 2016	https://deeptools.readthedocs.io/en/develop/#
cutadapt (v1.9.1)	Martin, 2011	https://github.com/marcelm/cutadapt
RSEM package (v1.2.31)	Li and Dewey, 2011	RRID:SCR_013027; https://github.com/deweylab/RSEM/releases/tag/v1.2.31
STAR alignment algorithm (v2.5.2a)	Dobin et al., 2013	RRID:SCR_004463; https://github.com/alexdobin/STAR/releases/tag/2.5.2a
DESeq2 package (v1.12.3)	Love et al., 2014	RRID:SCR_015687; https://www.rdocumentation.org/packages/DESeq2/versions/1.12.3
caret package	Kuhn, 2008	RRID:SCR_021138; https://CRAN.R-project.org/package=caret
scater package	McCarthy et al., 2017	RRID:SCR_015954; https://bioconductor.org/packages/release/bioc/html/scater.html
scran package	Lun et al., 2016	RRID:SCR_016944; https://bioconductor.org/packages/release/bioc/html/scran.html
Seurat (v3.2.2)	Stuart et al., 2019	RRID:SCR_016341; https://github.com/satijalab/seurat/releases/tag/v3.2.2
glmGamPoi package (v1.2.0)	Ahlmann-Eltze and Huber, 2020	https://bioconductor.org/packages/release/bioc/html/glmGamPoi.html
MAST package	Finak et al., 2015	RRID:SCR_016340; https://www.bioconductor.org/packages/release/bioc/html/MAST.html
SCDE R package (v1.99.4)	Fan et al., 2016; Kharchenko et al., 2014	RRID:SCR_015952; https://www.bioconductor.org/packages/release/bioc/html/scde.html
Txburst (Transcriptional burst kinetics inference)	Larsson et al., 2019	https://github.com/sandberg-lab/txburst
Other		
RPMI 1640 Medium, HEPES	ThermoFisher Scientific	Cat#22400089
RPMI 1640 Medium, no glucose	ThermoFisher Scientific	Cat#11879020
RPMI 1640 Medium, no glutamine	ThermoFisher Scientific	Cat#21870076
RPMI 1640 Medium, no phenol red (for live cell imaging)	ThermoFisher Scientific	Cat#11835063
RPMI 1640 Medium, no glutamine, no phenol red (for live cell imaging)	ThermoFisher Scientific	Cat#32404014

RESOURCE AVAILABILITY

Lead contact
Further information and requests for resources and reagents should be directed to and will be fulfilled by the lead contact, Paola Scaffidi (paola.scaffidi@crick.ac.uk).

Materials availability
Materials and reagents used in this study are listed in the key resources table. Plasmids generated in this study are available from the lead contact upon request. PDX-derived cells are covered by a Material Transfer Agreement and cannot be transferred.

Data and code availability

Z score tables from the large-scale fitness assays are available as supplemental data. Exome-seq, bulk RNA-seq, ChIP-seq, ATAC-seq and single-cell RNA-seq data have been deposited at NCBI-GEO (Super-Series GSE178643) and are publicly available as of the date of publication. Accession numbers are listed in the key resources table.

Any additional information required to reanalyze the data reported in this paper is available from the lead contact upon request.

EXPERIMENTAL MODEL AND SUBJECT DETAILS

Patient datasets

Pan-cancer cohorts. Nonsynonymous mutations affecting genes listed in Table S1 identified in 6 pan-cancer studies (Zehir et al., 2017; Robinson et al., 2017; Miao et al., 2018; Hyman et al., 2018; ICGC/TCGA Pan-Cancer Analysis of Whole Genomes Consortium, 2020; Nguyen et al., 2022) and corresponding variant allele frequency were retrieved from cBioPortal (Gao et al., 2013). For each gene, mutations classified as "driver" in cBioPortal (accessed on March 2022) and all truncating mutations were considered pathogenic. VAF values available in cBioportal are not corrected for purity and a low value does not necessarily mean that a mutation is subclonal. The VAF analysis mainly provided the rationale for performing a targeted analysis of subclonal mutations using multi-regions sequencing studies. The list of established tumor suppressor genes and oncogenes were obtained from Vogelstein et al. (2013) removing epigenetic regulator genes.

TRACERx cohort. Mutational data was obtained from Jamal-Hanjani et al. (2017) focusing on subclonal mutations affecting protein-coding regions, either nonsynonymous or synonymous.

LGG cohort. Mutational data displayed in Figure S1D was obtained from Table S1 in Suzuki e al., (Suzuki et al., 2015) focusing on nonsynonymous mutations with VAF <0.4. Phylogenetic trees from LGG and ccRCC (Gerlinger et al., 2014) were drawn based on published trees, visualizing mutations in epigenetic regulators retrieved from the corresponding supplementary data.

Cellular models

MEXF 2090, LXFL 1674, PAXF 1997, BXF 1352, CXF 269 derived cells were derived from the corresponding PDXs obtained from the Charles Rivers tumor model compendium (Table S2). All cell lines (and their derivatives) were cultured in RPMI 1640 (ThermoFisher Scientific, #22400089) with 10% fetal bovine serum (FBS), 100 U/ml penicillin, and 100 μg/mL streptomycin at 37°C in 5% C0$_2$. To enable efficient CRISPR-induced KO, MEXF 2090 and LXFL 1674 cells were transduced with a lentiviral pCW-Cas9 vector (Monserrat et al., 2021). Following a 7-day selection with 600 μg/mL hygromycin, clones with minimal background levels of Cas9 and responsive to induction with 1 μg/mL doxycycline were isolated.

Mice

NSG mice (NOD.Cg-Prkdc^{scid}Il2rg^{tm1Wjl}/SzJ) used in the *in vivo* competition experiment were obtained from the common Francis Crick colony. All animal studies were performed in accordance with the Francis Crick Institute Animal Welfare and Ethical Review Body and regulation by the UK Home Office project license PPL 70/8167 and PC2165EA4. Test naive male mice were used at 11–13 weeks of age for the experiment. Male mice were used to avoid possible interference of female menstrual cycle. The mice were housed in well-ventilated cages at a constant temperature and humidity (23 °C ± 2 °C, 50–60%) in a pathogen-free controlled environment, with a standard 12–12 h light–dark cycle, and food and water were provided *ad libitum*. The weight and signs of diseases were monitored in regular intervals.

METHOD DETAILS

Generation of KO lines

To generate cell lines expressing sgRNAs, cells were transduced with pLenti_BSD_sgRNA constructs (Henser-Brownhill et al., 2017) and selected with blasticidin (4 μg/mL) for 5 days. To induce gene KO, Cas9 expression was induced by the addition of doxycycline (1 μg/mL). sgRNA constructs were sourced from an available arrayed lentiviral sgRNA library (Henser-Brownhill et al., 2017). Lentiviral particles were produced by transfecting HEK293T packaging cells, in 96 well plates, at 80% confluence with 67.5 ng of the sgRNA lentiviral construct, 50.6 ng of psPax2 packaging plasmid (Addgene, #12260), 16.8 ng of pMD2G envelope plasmid (Addgene, #12259) and 15 ng pAdVantage (Promega, #E1711) at a ratio of 3:1 FugeneHD to DNA (Promega, #E2311). Approximately 24 and 48 h after transfection, the supernatant containing viral particles was recovered, filtered through a 0.45 μm filter (Millipore, #MSHVS4510), pooled together, and frozen at −80°C. After selection, expansion and induction of KO for 10 days, the libraries of KO populations were stored at −80°C in multiple aliquots. To freeze cells in 96-well format, cells were detached from the plate using 30 μL of trypsin per well. Following addition of 80 μL of FBS containing 10% DMSO, plates were sealed and stored at −80°C for up to 4 weeks. To thaw cells, plates were placed in a water bath at 37°C for a few seconds and spun for 5 min at 4°C after addition of 50 μL of medium to each well. Fresh medium (100 μL) was finally added to each well after removal of 120 μL of freezing medium. Isolated clonal KO populations were used for ChIP and ATAC experiments, after confirming that stress-resistant phenotypes were similar to the polyclonal populations. Experiments involving knock-out of *NELFA* were performed by transfecting synthetic guide RNAs (Edit-R crRNA, Horizon) (Table S7) in Cas9-expressing MEXF 2090 cells. *EZH2*- and *TNP2*-targeting crRNAs were used as positive and negative control, respectively. Each CRISPR RNA (crRNA) and the *trans*-activating CRISPR RNA (tracrRNA) were resuspended in

5× siRNA buffer (Horizon, #B-002000-UB-100) at a concentration of 20 μM. Each crRNA was then mixed with an equal amount of tracrRNA and the mix diluted 1:100 in Optimem medium (Gibco, #31985047). A total of 10 μL of the crRNA/tracrRNA mix was added to a well of a 96-well plate (to achieve a final concentration of 20 nM in a 100 μL of final volume) and mixed with 10 μL of transfection reagent (DharmaFECT Duo: 0.3 μL/96-well (Horizon, #T-2010-01)) diluted in Optimem. After 15 min, 4,000 cells resuspended in 80 μL of complete medium containing 1 μg mL−1 doxycycline were added to each well. After 2 days of transfection, cells were split 1:30 and plated in 6 replicate plates. Three days after transfection, cells from three plates were stained with SYTOX Green (d0) (ThermoFisher Scientific, #S7020 and #S11380 respectively) and medium was changed to L-glu-deprived medium (ThermoFisher Scientific, #21870076). At day 9, cells were fixed and stained with SYTOX Green (d9). Fitness was measured as fold change between d9 and d0.

Large-scale fitness assays

Plate layout: From the available sgRNA library (Henser-Brownhill et al., 2017), constructs targeting 318 genes, encoding *stricto sensu* epigenetic regulators were selected and arranged in eight 96-well plates (Corning, #3596). Each plate consisted of 40 KO populations in which distinct epigenetic regulators were inactivated, along with 20 negative control populations transduced with sgRNAs targeting 5 non-expressed genes, four replicates each. Multiple negative controls per plate were included to account for technical variability and well-effects, and to enable robust normalization of the observed phenotypes across plates and experiments. Each plate contained an *ARID2*-targeting sgRNA as an inter-plate standard. External wells were excluded and filled with PBS to avoid edge effects.

Assay pipeline: Multiple identical replicates, sufficient for the different treatments, were generated from each library plate. When the median cell count/well across plates reached ∼4000 cells, the plates were either grown under stressful conditions (see below) or maintained in unperturbed conditions. Over the course of the experiment one representative plate was monitored to confirm that the growth kinetics were as expected. At the indicated endpoints for each condition (see below) the population fitness was assessed by quantification of cell count: cells were fixed with 4% paraformaldehyde (PFA, Alfa Aesar, #43368) followed by permeabilization with 0.5% Triton X-100 in PBS and nuclei staining with SYTOX Green Nucleic Acid Stain (ThermoFisher Scientific, #S7020). Imaging and quantification were performed using an Incucyte S3 Live-Cell Analysis System.

Stress conditions: KO and control populations were cultured in the following conditions: a) unperturbed b) glutamine deprivation c) acidic environment and d) replication stress, with each stress applied at two distinct strengths. Glutamine deprivation was sustained for 3 or 7 days after glutamine removal. Media acidification was induced by addition of HCl to a final pH of 6.7 or 6.5, which resulted in a 40-60% reduction in cell counts after 3 days compared to untreated cells. To induce replicative stress, cells were cultured in the presence of 200 μM or 250 μM hydroxyurea (Sigma-Aldrich, #H8627) which resulted in 40% or 60% in cell counts after 3 days compared to untreated cells. Cell count for populations grown in unperturbed conditions was quantified at day 2. The endpoint of each treatment was determined based on when confluence was reached in fittest populations and depended on how severely cells were affected by each stress, with glutamine deprivation being the most deleterious stress. A survival benefit in at least one strength condition for each stress was considered as enhanced fitness. Experiments assessing the cellular response to thermal stress were performed by incubating MEXF 2090 cells at 43°C for 3 h, and then at 37°C for 9 days. To assess the response to oncogenic signaling inhibition, cells were cultured in the presence of 1 nM Buparlisib (Generon, #HY-70063-5mg) for 3 days. At the indicated endpoints for each condition, plates were fixed with 4% PFA followed by nuclei staining with SYTOX Green. Imaging and quantification were performed in Incucyte S3 Live-Cell Analysis System.

Filtering: Before quantifying normalized fitness, various parameters were assessed to remove: 1) wells containing cell clumps that would affect the measurement, identified by visual inspection of all plates; 2) outliers among replicates; 3) epigenetic regulators that are lowly expressed in MEXF 2090 (Log_{10} pseudo-counts <1) or LXFL 1674 (Log_{10} TPM <0.5) cells; 4) KO populations with severely compromised fitness in the unperturbed condition (20% reduction compared to the plate median for MEXF, 2090 and less than 20,000 cells at endpoint for LXFL 1674). The last step was performed to avoid inflated stress/unperturbed ratios. For steps 1 and 2, we excluded from the analysis 0.85% of imaged wells (61 out of 7200 total wells). 53 wells (87% of excluded wells) were excluded because they contained visible clumps of cells that would have confounded the analysis. The remaining 8 wells were excluded because they were highly inconsistent with the other two replicates (typically differing from the two consistent replicates more than 3 times their difference).

Data analysis. For each KO or control population the normalized fitness was derived from the stress/unperturbed ratio in cell count at endpoint. KO populations with enhanced or reduced fitness were defined based on the formula: $Z=(\chi-\mu)/\sigma$, where χ is the fitness of individual KO populations, μ is the mean fitness of negative controls, σ is the SD of the fitness of negative controls. Populations exhibiting enhanced or reduced fitness were defined as those with a *Z* score > 1.645 or < -1.645 (90% confidence interval), respectively. Since we used a high ratio of sample vs negative controls (2:1) and the *Z* score includes information on confidence level, correction for multiple comparisons was not required.

Validation fitness assay

Validation fitness assays were performed in a similar way as the large-scale assays, either measuring cell count over time using replicates fixed at various time points, or at endpoint. Population growth was quantified by normalizing the average cell count at each time point to the pre-treatment count (d0). In experiments where the population growth was monitored over several weeks, smoothing was applied to the curves to account for technical noise introduced by media change. Throughout the study, selection of genes

for targeted analysis was driven by three factors: (i) the need of including epigenetic regulators representative of multiple functional classes, to be able to assess network-level effects; (ii) the decision to not limit the analysis to "top performers" and instead assess populations exhibiting varying degree of stress-resistance, including mild phenotypes (e.g. HIST1H1B-KO cells); (iii) the complexity of the assay performed, which affected the number of populations that we could analyze in the different experiments. When using inhibitors, availability of specific compounds was an additional criterion for selection.

Treatment with epigenetic inhibitors

MEXF 2090, PAXF 1997, BXF 1352 and CXF 269 cells were pre-treated for 3 days before being exposed to stress, and drugs and media were replaced every 3 days over the course of the experiment. Variable population growth rate and sensitivity to nutrient deprivation contribute to the effect size detected in each model. When assessing the reversibility of the stress-resistant phenotype, MEXF 2090 cells were grown for 9 days in the presence of the inhibitors, and for an additional 9 days in the absence of the compounds (Figure 4B). When assessing the effect of pre-treatment, MEXF 2090 were pre-treated for 3 days, then drugs were withdrawn and cells were left to recover for 2 days before being exposed to stress (Figure S2G). Concentrations of the inhibitors used are as follows: RGFP9665 [5μM (MEFX, 2090); 1.25 μM (PAXF, 1997; BXF 1352, CXF 269)]; Tubastatin A [2.5 μM (MEFX, 2090); 5 μM (PAXF, 1997; BXF 1352, CXF 269)]; EX 527 (SEN0014196) [2.5 μM (MEFX, 2090); 1.25 μM (PAXF, 1997; BXF 1352, CXF 269)]; EPZ004777 [2.5 μM (MEFX, 2090)]; MM-102 [2.5 μM (MEFX, 2090)]; WM-8014 [5 μM (MEFX, 2090)], GSK126 [1.25 μM (MEFX, 2090; PAXF, 1997; BXF 1352, CXF 269)]; Quisinostat [5 nM (MEFX, 2090); 1 nM (BXF 1352, CXF 269) 0.5 nM (PAXF, 1997)]; JIB-04 [5 nM (MEFX, 2090)].

Proliferative and apoptotic fractions

Two hours before the endpoint, populations were pulsed with 10 μM EdU and 5 μM of Ac-DEVD-NucView488. (Cen et al., 2008) Live cell imaging of Caspase 3 activity was performed using an Incucyte S3 Live-Cell Analysis System. Subsequently, cells were fixed with 4% PFA followed by EdU staining by using the Click-iT EdU Cell Proliferation Kit (ThermoFisher Scientific, #C10340) as per manufacturer's protocol, and SYTOX Green staining for nuclei quantification.

Cell cycle analysis

MEXF 2090 cells were grown in unperturbed condition for 3 days. One-hour prior collection, cells were pulsed with 25 μM EdU. Cells were detached, fixed in 4% PFA and permeabilized in 0.5% Triton X-100. EdU was detected using a biotin-azide click reaction by incubating cells in 100 mM Tris HCl pH 7.6, 4 mM CuSO4, 5 μM M Sulfo-Cyanine5 Azide (Lumiprobe, A3330), 100mM Sodium Ascorbate for 5 min at room temperature. After washing, cells were resuspended in 1 μM/mL DAPI and analyzed by flow cytometry.

ATP assays

MEXF 2090 were plated in two identical replicates in 96well-plate. After 3 days of growth, one plate was lysed using CellTiterGlo reagent (Promega, G9242) following manufacturer instructions. Briefly, culture medium was removed, and cells were incubated with a 1:1 mixture of CellTiterGlo reagent and medium with gentle shaking. After 10 min, the solution was transferred to a white 96 well plate and luminescence was measured using a PHERAstar microplate reader. To infer the ATP levels per cell, the replicate plate was fixed with 4% PFA, permeabilized and stained with SYTOX Green Nucleic Acid Stain (Thermo Fisher Scientific, S7020). Imaging and quantification were performed using an Incucyte S3 Live-Cell analysis system to obtain the number of cells per well. ATP levels per cells were then calculated dividing luminescence intensity by the number of cells per well.

Sensitivity assays

To assess the basal sensitivity of control and epigenetically-disrupted MEXF 2090 cells to CDK9 and BET inhibitors, cells were treated for 48 h with compounds or DMSO as control: CDK9i: 5,6-Dichlorobenzimidazole 1-β-D-ribofuranoside (DRB) 15 μM (Merck, F3055-5MG) and Flavopiridol hydrochloride hydrate 1 nM (Merck, F3055-5MG). BETi: JQ1 1 μM (Merck, SML1524–5MG). At the indicated endpoint, cells were fixed with 4% PFA followed by nuclei staining with SYTOX Red. Imaging and quantification were performed in Incucyte S3 Live-Cell Analysis System. The percentage of killing was calculated by comparing drug-treated cells with DMSO-treated cells. In parallel, control MEXF 2090 cells and KO populations were cultured for 8 days in nutrient-deprived condition to select stress-resistant cells. At day 8, cells were split at equal density and grown overnight in unperturbed conditions. The following day, stress-resistant cells were treated for 48 h with CDK9 and BET inhibitors or DMSO as control and sensitivity assay was calculated as stated above.

In vitro competition assays

MEXF 2090 cells were transduced with lentiviral constructs expressing GFP-NLS (pTRIP-SFFV-EGFP-NLS, Addgene #86677) (Raab et al., 2016), or mCherry-NLS (pTRIP-SFFV-mCherry-NLS). To generate pTRIP-SFFV-mCherry-NLS, mCherry was amplified from pUAS-mCherry-NLS (Addgene #87695) (Zhang et al., 2017) by PCR (forward primer: TAGCGGATCCATGGTGAGCAAGGGCGAG, reverse primer: AGGTCTCGAGCGCCCGACTCTAGATTATAC) and cloned in the pTRIP-SFFV expression vector after GFP removal by BamHI-XhoI digestion. Seven days after infection, cells expressing similar levels of the fluorescent proteins were isolated by flow cytometry. mCherry-labelled lines were transduced with sgRNA constructs targeting epigenetic regulators, while GFP-labelled cells with sgRNAs targeting the non-expressed gene *TNP2*. After 10 days of blasticidin selection and induction of KO through doxycycline treatment, mCherry-labelled KO populations were mixed with GFP-labelled control cells in equal quantities and seeded in 96-well

plates at a density of 3000 cells per well. A mix of GFP- and mCherry labeled control cells was used as a baseline to account for possible differential fitness of the two labeled lines. Twenty-four hours after plating, the medium was refreshed with phenol-free RPMI lacking L-glutamine (ThermoFisher Scientific, #32404014). Live cell imaging was performed at 12-h intervals using an Incucyte S3 Live-Cell Analysis System. During the course of the experiment, the media was refreshed every 3 days. After 12 days in nutrient deprivation, the mCherry to GFP ratio was calculated and normalized to the pre-treatment ratio.

In vivo competition assays

MEXF 2090 cells transduced with sgRNAs targeting either *EZH2* or *TNP2* (non-expressed control gene) and treated with doxycycline for 10 days were mixed at equal ratio and injected in NOD.Cg-Prkdc^scid Il2rg^tm1Wjl/SzJ (NSG) mice obtained from the common Francis Crick colony. 5 x 10^5 cells from the mix were intradermally injected in both flanks of 11–13-week-old male NSG mice in 50 μL of PBS. Approximately 3 weeks after injection mice were randomly segregated in two groups and treated with either Bevacizumab (Stratech, #A2006-SEL-5mg; twice a week i.p. at the dose of 2 mg/kg or 8 mg/kg) or vehicle. Tumor volume was measured twice a week using electronic calipers until animals were humanely killed approximately 5 weeks after injection. At the endpoint, tumors were harvested and the relative abundance of *EZH2*-KO and control cells was estimated by next-generation sequencing of the sgRNAs amplified from tumors. To do so, tumors were cut into small pieces of ∼2–3 mm in length, transferred into gentleMACS M tubes (GentleMACS, #130-096-335) containing two volumes of ATL buffer supplemented with 1:10 proteinase K (Qiagen, #69506) and blended at high speed with a gentleMACS dissociator (RNA_01.01 Program). (Morales Torres et al., 2020) gDNA from tumors and the injected cells was extracted using a DNeasy Blood & Tissue kit as per manufacturer's protocol (Qiagen, #69506). NGS libraries were prepared by performing a two-step nested PCR using Herculase II Fusion Enzyme Kit (Agilent Technologies, #600679) and primers listed in Table S7. To ensure efficient amplification of the sgRNAs, multiple PCR reactions were run for each sample, using a maximum of 1 μg gDNA in 50-μL reactions with 20 cycles of amplification. Following the first round, the PCR product was cleaned using QIAquick PCR Purification Kit (Qiagen, #28104) and 1/50 of the reaction was used as template for the second PCR, run for 28 cycles. Final products were run on a 2% agarose gel and purified using a QIAquick gel extraction kit (Qiagen, #28706). Libraries were sequenced on the Illumina MiSeq using the MiSeq Reagent Nano Kit V2 (Illumina, #MS-102-2001) with 250 bp paired end reads and generated approximately 6000 251bp reads per sample. Raw reads were trimmed with the fastx_trimmer tool available within the FASTX-Toolkit (version 0.0.14) http://hannonlab.cshl.edu/fastx_toolkit using the parameters "-f 122 -L 141 -m 20″ to extract the sgRNA sequence. These were then mapped to a reference consisting of the 14 guide sequences of interest using BWA (version 0.5.9-r16) (Li and Durbin, 2009) with the parameters "-l 20 -k 4 -n 4". sgRNA counts were obtained after filtering the mapped reads for those that had zero mismatches, and mapped to the sense strand of the guide sequence. To quantify the relative abundance of sgRNAs in each condition, raw reads for each sgRNA were normalized to the overall read counts.

Immunofluorescence microscopy

Immunostaining of cultured cells was performed using standard protocols as described in (Monserrat et al., 2021) using anti-lamin A/C (Santa Cruz Biotechnology, #sc-7292, 1:200), anti-H3K27me3 (EMD Millipore, #07-449, 1:400), anti-H4K16ac (Cell Signaling Technology, #2591, 1:500) primary antibodies and relevant fluorescent secondary antibodies. Imaging was performed using either an IncuCyte S3 system or an Axiovert Zeiss confocal microscope. For analysis of tumors, portions of tumors harvested from mice were fixed in 10% formalin and embedded in paraffin. Sections were deparaffinized with xylene and rehydrated in an ethanol gradient. Antigen-retrieval was performed for 20 min at 95°C in citrate buffer. Slides were then blocked, incubated overnight with anti-H3K27me3 antibody (1:200) or phospho-S6 Ribosomal Protein (Ser235/236) (Cell Signaling Technology, #2211) at 4°C, washed, incubated with the secondary antibodies (ThermoFisher Scientific, anti-rabbit Alexa flour 488, #A-21206 or anti-rabbit Alexa flour 568, #A10042) for 1 h at room temperature, washed 3 times with PBS, incubated with DAPI and mounted with Pro-Long Gold Antifade Mountant (ThermoFisher Scientific, #P36934). Slides stained with only the secondary antibody were used as a negative control. Stained slides were imaged using an Olympus VS120 Slide Scanner and images were processed with QuPath-0.2.2 (Bankhead et al., 2017) and quantified with ImageJ 1.45s.

Clonogenic assays

For qualitative assessment, 1500 cells were plated in 6-well plates, while for quantification 10 cells/well were seeded in 96-well plates. After 24 h, the medium was refreshed to RPMI 1640 without glutamine (ThermoFisher Scientific, #21870076) and cells grown for 12 days until visible colonies appeared. Media was refreshed every 3 days. Cells were fixed with 4% PFA, permeabilized with 0.5% Triton X-100 in PBS stained with SYTOX green and imaged using an Incucyte S3 Live-Cell Analysis System.

Live-cell imaging

MEXF 2090 were modified to express the FRET-based glucose biosensor, which indicates relative preference for glycolysis and OXPHOS in living cells. (Kondo et al., 2021) The PiggyBac transposon containing the FRET biosensor (Kondo et al., 2021) was co-transected with a plasmid expressing the PB transposase (PBase) (Liang et al., 2009) at a 1:3 ratio using the FuGENE HD reagent as per manufacturer's protocol (Promega, #E2311). After 7 days, citrine-expressing cells were isolated by flow cytometry. For live-cell imaging, cells were plated in optical grade 96-well microplates (GBO, #655090). Two hours before imaging, the media was replaced with phenol-free RPMI with or without L-glutamine (ThermoFisher Scientific, #11835063 and #32404014, respectively). Cells were imaged at 15-min intervals for 24 h using an inverted Zeiss LSM 880 confocal microscope and Zeiss Zen software (v2.3).

A Plan-Apochromat 20x/0.8 NA objective lens was used and the emission signals were detected using the internal 32-channel GaAsP detector. Excitation light from an argon ion laser set to 3.5% was passed through a 458/514/561/633 multiple beam splitter and emission light was detected between 464 and 506 nm for eCFP and 517-571 nm for sensitized emission (FRET). Image acquisition settings were set to 512 x 512 pixels, zoom 0.6, 8.24 μs pixel dwell and line 4 averaging. Master gain for eCFP detection was set to 850 and 750 for citrine detection. Digital gain was set to 1.0 for both and digital offset was set to 0 for both. 3 x 2 tiling with 5% overlap followed by stitching was used to capture a rectangular field of view. The FRET ratio per cell was calculated from perinuclear areas (4x4 pixels) by dividing the total intensity in the FRET channel by the total intensity in the eCFP channel. For time-lapse single cell analysis, individual cells were manually tracked and the FRET ratio at each time point was calculated as described above. The measurements from time points overlapping with active cell divisions were discarded and replaced with the average of 6 time points (three prior and three after) flanking mitosis. The FRET biosensor is very sensitive to even minor changes in metabolic states induced by various factors, including cell density and motility. (Kondo et al., 2021) Thus, small variations in the number or distribution of seeded cells could account for the different basal level detected in Figure 4F. Other technical details, such as position of the well within the 96-well plate, which influences gas exchange and temperature equilibration after change to nutrient deprived medium, could contribute to the small initial difference. Independently of the source of variation in the baseline, 3h after media change, both samples exhibited comparable FRET signal, which increased at distinct rates. To assess mitochondrial activity, cells were pulsed with 100 nM of Tetramethylrhodamine ethyl ester perchlorate (TMRE, ThermoFisher Scientific, #T669). After 30 min, TMRE fluorescence was imaged and quantified using an Incucyte S3 Live-Cell Analysis system.

RT-qPCR and nascent RNA analysis
RNA was extracted using a RNeasy Plus Micro Kit (Qiagen, #74034) according to the manufacturer's guidelines. For standard analysis of RNA levels, 500 ng of RNA was reverse transcribed using a High Capacity cDNA Reverse Transcription Kit (ThermoFisher Scientific, #4368814) as per manufacturer's instructions. cDNA was diluted 1/10 and used as input for RT–qPCR using SsoAdvanced Universal SYBR Green Supermix (Bio-Rad, #172-5274) on a CFX96 real-time PCR detection system (Bio-Rad). *PPIA* was used as reference gene for normalisation. For nascent RNA analysis, genomic DNA was removed first by passing cell lysates into gDNA eliminator spin columns and then by treatment of eluted RNA with TURBO DNase for 20 min (ThermoFisher Scientific, #AM2238). cDNA was prepared from 1 μg or 2 μg of extracted RNA and nascent transcripts detected using intronic primers. *C1ORF43* was used as a reference gene for normalisation. Primers used for RT–qPCR in this study are listed in Table S7.

Chromatin immunoprecipitation (ChIP)
MEXF 2090 cells grown in either unperturbed conditions or under glutamine deprivation for 2 days were cross-linked using 1% formaldehyde for 10 min. The reaction was stopped by incubation for 5 min with 0.125M glycine. Cell pellets were washed twice with cold PBS containing protease inhibitor and ChIP performed as previously described. (Simeoni et al., 2021) 3.5 million cells were used for Pol II Ser2 ChIP-qPCR, while 2 million for ChIP-seq. Briefly, nuclear lysates were sonicated using a Bioruptor Pico for 6 cycles, 30s ON, 30s OFF settings. Immunoprecipitation was performed overnight at 20 rpm and 4°C, with 20μL Dynabeads (Protein G, ThermoFisher Scientific, #10003D) per 2 μg antibody: ChIP Grade Rabbit monoclonal [EPR18855-87] to RNA polymerase II CTD repeat YSPTSPS (phospho S2) – (Abcam, #ab238146-); Rabbit monoclonal anti-trimethyl-Histone H3 (Lys27) (C36B11) (Cell Signaling Technology, 9733); Rabbit monoclonal anti-acetyl-Histone H3 (Lys27) (D5E4) (Cell Signaling Technology, #8173); Rabbit polyclonal anti-monomethyl- Histone H3 (Lys4) (Abcam, ab8895); Rabbit polyclonal anti-trimethyl- Histone H3 (Lys4) (Abcam, ab8580). After washing four times with RIPA buffer (50 mM HEPES pH7.6, 1 mM EDTA, 0.7% Na deoxycholate, 1% NP40, 0.5 M LiCl), chromatin IP-bound fractions were extracted at 65°C for 30 min with elution buffer (50 mM TrisHCl pH8, 10 mM EDTA, 1% SDS) vortexing frequently. RNaseA (0.2 mg/mL) and proteinase K (0.2 μg/mL) were used to eliminate any RNA or protein from the samples. Finally, DNA was extracted using phenol:chloroform:isoamyl alcohol extraction and precipitated with ethanol (adding two volumes of ice-cold 100% ethanol, 20 μg/μL glycogen and 200 mM NaCl) for at least 1 h at −80°C. Pellets were washed with 70% ethanol and eluted in 50 μL 10 mM TrisHCl pH8.0. For ChIP qPCR, assays were performed on a CFX96 real-time PCR detection system (Bio-rad) using SsoAdvanced Universal SYBR Green Supermix (Bio-rad). Values for each gene were normalized to input DNA and expressed as relative to the unperturbed conditions. Primers used were designed in the last intron of each gene and are listed in Table S7. For ChIP-sequencing, libraries were made using NEBNext Multiplex Oligos for Illumina (96 Unique Dual Index Primer Pairs) kit (NEB, E6440S) following manufacturer's instructions and were sequenced on an Illumina NovaSeq platform.

Assay for transposase-accessible chromatin (ATAC)
ATAC-seq was carried out as previously described with minor modifications. (Corces et al., 2017) Briefly, 50.000 MEXF 2090 cells were pelleted by centrifugation and resuspended in 50 μL of cold lysis buffer (10 mM Tris–HCl pH 7.4, 10 mM NaCl, 3 mM MgCl2, 0.1% NP40, 0.1% Tween 20, and 0.01% digitonin). After incubation on ice for 3 min, 1 mL of lysis buffer without NP40 and digitonin was added. Nuclei were pelleted by centrifugation for 10 min at 500 g, 4°C. The supernatant was discarded, and nuclei were resuspended in 50 μL of reaction buffer containing 2.5 μL of Tn5 transposase, 25 μL of 2× TDE buffer (20 mM Tris–HCl, pH 7.6, and 10 mM MgCl2, 20% Dimethyl Formamide), 16.5 μL of PBS, 0.5 μL of 1% digitonin, and 0.5 μL of 10% Tween 20. The reaction was incubated at 37°C for 30 min with mixing (600 RPM). Then, tagmented DNA was cleaned up using Zymo DNA concentrator (Zymo Research, D4004) and amplified by PCR using NEBNext High-Fidelity 2X PCR Master Mix (M0541S). PCR was run as follows: 72°C for 5 min, 98°C for 30s, 14 cycles of 98°C for 30 s, 63°C for 30 s and 72°C for 60s, followed by a final extension at 72°C for 5min.

Fragments smaller than 600 bp were isolated using SPRI cleanup (Beckman Coulter, A63881), and libraries were sequenced on an Illumina NovaSeq platform. The Tn5 enzyme was produced by the Structural Biology STP in the Francis Crick Institute following published protocols. (Hennig et al., 2018) For oligo sequence, see Table S7.

Exome-seq

Genomic DNA (gDNA) was isolated from clonal lines derived from MEXF 2090 and LXFL 1674 cells. Cells grown in 96-well plates were washed once with PBS, lysed with 50 μL Bradly Lysis buffer (10 mM Tris-HCl pH7.5, 10 mM EDTA, 0.5% SDS, 10 mM NaCl) supplemented with 1 mg/mL Proteinase K (Qiagen, #19131) and incubated overnight at 60°C. DNA was precipitated by addition of 100 μL of ice-cold EtOH/NaCl (75 mM NaCl in 100% EtOH) followed by vigorous mixing, incubation at room temperature for 30 min and centrifugation at 3000 x g for 20 min. The pellet was washed twice with 100 μL of 70% EtOH followed by centrifugation at 3000 x g for 10 min. DNA was resuspended in 30 μL of warm TE pH 8.0 after incubation at 56°C for 10 min. For whole exome sequencing, gDNA samples were quantified using a QuantiFluor dsDNA system (Promega, #E2670) on the GloMax Multi Detection System following the manufacturer's guidelines. Sample quality was assessed using the Genomic DNA ScreenTape System run on the TapeStation 4200 according to the manufacturer's instructions (Agilent Technologies, #5067-5365; #5067-5366). Subsequently, gDNA was fragmented using Covaris LE220-plus focused ultrasonicator and then prepared into libraries using the NEBNext Ultra II DNA library prep kit (NEB, #E7645S) according to manufacturer's instructions. Libraries were then combined in 8-plex and exonic regions enriched via hybridization using the Twist Human Core Exome kit according to the manufacturer's instructions (#100578; #101174; #100254). Libraries were sequenced on the HiSeq 4000 using paired end 100 bp reads.

Bulk RNA-seq

Transcriptomic analysis was performed in 6 different KO populations of MEXF 2090 cells in which *EED*, *EZH2*, *HIST1H1B*, *SMARCD1*, *SUZ12* and the non-expressed gene *TNP2* were targeted and that were grown under nutrient deprivation for 12 days. Four and six replicates of unperturbed and nutrient-deprived cells, respectively, grown in distinct wells of 96-well plates were pooled and total RNA extraction was performed using a RNeasy Plus Micro kit. Total RNA was quantified using an RNA QuantiFluor RNA system (Promega, #E3310) on the GloMax Multi Detection system following the manufacturer's guidelines. RNA quality was assessed via the High Sensitivity RNA ScreenTape using the TapeStation 4200 (Agilent Technologies, #5067-5579). RNA was normalized to 30 ng and used for cDNA synthesis and library preparation using the QuantSeq 3′ mRNA-Seq FWD kit (Lexogen, #015) according to the manufacturer's instructions. Libraries were sequenced on the Illumina HiSeq 4000 with single ended reads.

scRNA-seq

MEXF 2090 cells were transduced with lentiviral constructs expressing sgRNAs whose scaffold was modified to contain the Capture Sequence 1 that is compatible with the 10x Genomics Feature barcoding technology (Table S7). To generate the modified constructs, synthetic sgRNA scaffolds containing the Capture sequence 1 (Genscript) were cloned into the pLenti-BSD-sgRNA plasmid after removal of the pre-existing scaffold by BstBI-NsiI digestion. To maximize editing efficiency, the KO populations also contained the respective pools of unmodified sgRNAs sourced from the available sgRNA-library. (Henser-Brownhill et al., 2017) Six replicates for each KO population, grown in different wells of 96 well plates, were cultured under nutrient deprivation for 12 days and pooled at endpoint. A reverse time-course scheme was followed to allow simultaneous collection of d0 (unperturbed) and d1, d2 and d12 samples (nutrient-deprived) (Figure S5A). Control and KO populations from each timepoint were pooled together prior to the library preparation step to minimize technical variability. Single cell mRNA-Seq was carried out using the 10x Single Cell Gene Expression kit v3.1 with Feature Barcoding technology for CRISPR Screening according to the manufacturer's instructions (10x Genomics, #CG000205). Briefly, cell suspension was counted and assessed for viability using an EVE automated cell counter (NanoEntek). Approximately 10,000 cells (mix of control and KO populations), per time point, were loaded into the 10x Chromium chip. GEM generation, barcoding, cDNA synthesis and clean-up was carried out as per the 10x protocol. Subsequently, the gene expression and feature barcoding libraries were separated by size selection and sequenced on the HiSeq 4000 according to the 10x guidelines. For the gene expression and the CRISPR libraries, approximately 336 and 268 million reads were acquired, respectively (mean values per time point). This resulted in a sequencing depth of ∼87.000 reads/cell and subsequent detection of ∼5800 genes/cell. Multiple sequencing runs were performed and aggregated using the built-in pipeline of 10x Genomics' software (CellRanger 3.0.2).

QUANTIFICATION AND STATISTICAL ANALYSIS

Analysis summary

Experimental sample sizes were based on the variability observed in pilot experiments. The type of statistical tests performed in this study, whether they were one- or two-tailed, the value of N, and what N represents are indicated in the main text or in figure legends. Unless otherwise stated, all values are the average of individual values ±SEM from at least three biological replicates. Values of burst parameters were log-transformed prior to ANOVA to favor normal distributions. A logistic transformation was applied to the cell fractions detected in the *in vivo* competition assays prior to one-sample t-test to account for the fact that fractions are bounded above and below. Statistical analysis was performed using the indicated NGS-related packages or GraphPad software.

Exome-seq analysis

Trimmed (Trim Galore v0.6.4_dev) 101 basepair paired-end reads were aligned to human genome reference sequence GRCh38 using BWA mem (v0.7.17-r1188). (Vasimuddin et al., 2019) A mean alignment rate of 68,686,981 properly paired read pairs per sample was obtained across the 10 samples (SD 17,806,612) with a mean insert size of 175.14 (mean SD 69.13). The mean coverage across at least 50% of the exome was 176.8. Duplicates were marked using GATK MarkDuplicatesSpark (v4.1.7.0) (Van der Auwera et al., 2013) and base quality scores recalibrated using GATK BaseRecalibrator and ApplyBQSR (GATK v4.1.7.0). SNVs and indels were called using Strelka2 (v2.9.10). (Saunders et al., 2012) Genome sequence, indices and dbSNP calls were obtained from the GRCh38 GATK bundle. SNVs and Indels were annotated using SnpEff (v4.3t, SnpEff DB version GRCh38.86). (Cingolani et al., 2012) The nfcore/sarek pipeline (v2.6.1) (Garcia et al., 2020; Ewels et al., 2020) with Nextflow (v20.11.0-edge) (Di Tommaso et al., 2017) was used to run the analysis end to end. Read depth varied from 3 to 671 per gene. Mutations with a read count <50 reads (lower 10%) for either allele were excluded due to low coverage.

Bulk RNA-seq analysis

RNA sequencing was carried out on the Illumina HiSeq 4000 platform in multiple runs and typically generated ~11 million 76/101bp strand-specific single-end reads per sample. Adapter trimming was performed with cutadapt (version 1.9.1) (Martin, 2011) with parameters "–minimum-length = 25 –quality-cutoff = 20 -a AGATCGGAAGAGC". The RSEM package (version 1.2.31) (Li and Dewey, 2011) in conjunction with the STAR alignment algorithm (version 2.5.2a) (Dobin et al., 2013) was used for the mapping and subsequent gene-level counting of the sequenced reads with respect to hg19 RefSeq genes downloaded from the UCSC Table Browser (Karolchik et al., 2004) on 7th June 2017. The parameters used were "–star-output-genome-bam –forward-prob 1". Differential expression analysis was performed with the DESeq2 package (version 1.12.3) (Love et al., 2014) within the R programming environment (version 3.3.1). (Team, 2015) An adjusted p value lower than 0.01 was used as the significance threshold for the identification of differentially expressed genes. Pseudocount values estimated with the DESeq2 package were used to identify non- and lowly-expressed genes in MEFX 2090 cells, as transcript per million (TPM) values normalized to gene-length are not suitable for 3′-mRNA-seq datasets. Expression values (TPM) for LXFL 1674 cells were sourced from the publicly available Oncotest-Charles River dataset.

Gene set enrichment analysis (GSEA)

Gene set enrichment analysis (GSEA) (version 4.0.3) (Subramanian et al., 2005) of pre-ranked gene lists (either whole transcriptomes or identified meta-signatures) was performed using the Wald statistic focusing on MSigDB (version 7.4) hallmark, curated and GO gene sets. All parameters were kept as default except for enrichment statistic, which was set to *classic*. To assess the enrichment of signatures in HVGs and HFGs, the "compute overlaps" function of MSigDB was used, focusing on the hallmark gene sets and setting a threshold for biological significance at p value $\leq 10^{-10}$.

scRNA-seq analysis

sgRNA demultiplexing and cell type assignment

After removal of cells with empty CRISPR guide genes, a multinomial logistic regression model was applied to assign cell labels. Cells with only one CRISPR gene counts different from zero were assigned to the corresponding cell type, and used to fit logistic regression model

$$f_{i,k} \;=\; \beta_{0,k} + \sum_{j=1}^{6} \beta_{j,k} * g_{i,j}$$

where $f_{i,k}$ is the probability that cell *i* is assigned to cell type *k*, and $g_{i,j}$ represents the normalised *j*-th CRISPR counts of the *i*-th cell. CRISPR gene counts were normalized by dividing by the total counts of the gene across all cells. The model, fitted using *caret* package (Kuhn, 2008) for R, was used to predict the assignment probability of cells with two or more non-zeros CRISPR gene counts. Cells with a predicted probability greater than 95% were assigned to the corresponding label. The other cells were considered ambiguous and therefore removed from the dataset.

Filtering

An iterative procedure was applied to identify and remove highly-stressed, low-quality cells and lowly-expressed genes from the count table of the labeled cells at the four time points. At each iteration, the procedure involved: a) removal of genes detected in less than 20 cells across all time points, b) removal of cells with small total counts and a small number of detected genes (lower than 3 median absolute deviations (MADs) from the median) using the *scater* package (McCarthy et al., 2017) for R, c) removal of cells with a high percentage of mitochondrial genes counts (higher than 3 MADs from the median). (Ilicic et al., 2016) After identification and quantification of unhealthy low-quality cells in each cell population, those cells were removed from the downstream analysis.

Normalization

The filtered dataset was normalized using the *scran* package (Lun et al., 2016) for R. The scaling factors were firstly estimated on clusters identified by the function *quickCluster*, and then deconvoluted using the function *calculateSumFactors*. The same results were obtained by using the function *computeSumFactors*. The normalization affected the dataset minimally (median scaling factor across all cells: 0.89, with 50% of cells between 0.67 and 1.23), confirming that the experimental design minimized technical

variability (Figure S5A). The log$_2$-transformed normalized counts were used as features for the subsequent modeling, except for the burst kinetics analysis, which used the raw data, and the variance analysis where normalization was carried out with the PAGODA algorithm.

Dimensionality reduction and differential gene expression analysis

Dimensionality reduction was performed using Seurat (version 3.2.2) (Stuart et al., 2019) after merging all samples into one Seurat object to allow projection of all samples onto the same UMAP space, and using stress-responsive genes defined at d1 and d2 (early stress response). For differential gene expression analysis, pre-filtered single cell samples relevant for each comparison (either all cell populations at each time-point, or one cell population across time) were merged and differentially expressed genes were identified using the FindMarkers function from Seurat. For time-point comparisons, all time points were compared to the d0 sample. In addition, pairwise comparisons between consecutive time points were made (d2 vs d1, d12 vs d2) to assess progressive changes or reversal of gene mis-expression. For cell-population comparisons, all KO populations were compared to control cells within each time point. These comparisons were repeated using the glmGamPoi Biocnductor package (1.2.0) (Ahlmann-Eltze and Huber, 2021) correcting for cell cycle phase which was calculated using the CellCycleScoring function and cell cycle phase specific genes provided by Seurat. 100 cells were sampled from each group prior to analysis to speed up the computation. Statistical significance of the differences was assessed by non-parametric Wilcox test using default parameters followed by Bonferroni correction for multiple testing (based on all tested genes). Differentially expressed genes were defined as genes with an FDR <0.01 between conditions using cell-cycle corrected data.

Cell clustering and identification of KO-enriched or control-enriched subpopulations

The general procedure to determine the sub-population-specific genes consisted of two steps: firstly, each pair of KO and control cell populations at d12 were clustered based on their gene expressions, and the differentially expressed genes between cell clusters enriched with either population were determined (see Figure 5C). Secondly, the corresponding signatures defining each enriched cluster were merged through hierarchical clustering across all pairwise comparisons to define gene signatures shared by KO- or control-enriched subpopulations. More in detail, for each cell population P, the $N^{(P)} \times M$ gene expression matrices $X^{(P)}$ were defined, where $N^{(P)}$ represents the size of P, and M represents the number of genes. For each KO population, we then performed a pairwise modeling with the control cells using the $N^{(d12)} \times M'$ matrix, $\mathbf{X}^{(d12)}$, where $N^{(d12)} = N^{(KO)} + N^{(cntr)}$, consisting of the expression of the most variable genes (VGs) within the merged cell populations. VGs were defined by applying the method described in Brennecke et al. (2013) to the normalized (not log2-transformed) gene expression values. Principal Component Analysis (PCA) dimensionality reduction was applied to the merged cell cycle-corrected VG data to generate the feature matrix used for each comparison. A number $d < M$ of PCA dimensions were retained, corresponding to the elbow of the variance explained var_{exp} by each component. The elbow point was defined as the farthest point of the var_{exp} curve from the line connecting the points $\boldsymbol{P}_0 = (1, var_{exp}(PC1))$ and $\boldsymbol{P}_1 = (PC_{max}, var_{exp}(PC_{max}))$, with $PC_{max} = 200$. The $N^{(d12)} \times d$ PCA scores matrix T was used to determine the cell clusters. For visualization purposes, a 2-dimensional t-SNE mapping was obtained from the scores $\mathbf{T}$, with a perplexity value set to 30. PCA and t-SNE dimensionality reduction were performed using the *Seurat* (version 3.2.2) package for R. Cell clustering was performed via nearest-neighbors method (num. neighbors = 20, tree pruning = 1/15) (Jarvis and Patrick, 1973) followed by graph partitioning through the functions available in *Seurat*. Consensus clustering (Monti et al., 2003) and detection of the optimal resolution were performed with in-house developed R scripts. Enrichment analysis of each cell population in each cell cluster was performed by hypergeometric test: for each cell type, p values were calculated from the cumulative distribution function, using the *phyper* function for R and corrected for multiple testing using Benjamini-Hochberg method. Only clusters significantly enriched for at least one a cell population (adjusted p value < 0.05) were used in the following steps of the analysis. Gene signatures defining each KO- or control-enriched clusters consisted of DE-Gs identified by *MAST* (Finak et al., 2015) between each cell cluster and all other cells of the pair merged set. Genes with FDR <0.05 and a non-zero log$_2$-fold-change (with a non-zero-crossing 95% confidence intervals) were considered differentially expressed and used to characterize the cells belonging to the cluster. After performing the clustering analysis on cells for all KO-control comparisons, all the identified cell-cluster-specific gene signatures were clustered together to identify DE-Gs shared by different cell-clusters. To increase the robustness of the results, signatures consisting of less than 50 DE-Gs or that corresponded to cell clusters with a size smaller than 5% of the pooled set size were removed. The gene signatures were defined as vectors where each element corresponded to the product of the point estimate of the log2-fold-change and the significance (equal to $-\log_{10} p$) of each DEG, as determined by *MAST*. All non DEGs were assigned a signature value equal to 0. Gene signatures were clustered using a hierarchical clustering. Spearman's correlation was used as similarity measure and the optimal linkage corresponded to the maximum cophenetic correlation coefficient (Sokal and Rohlf, 1962). The optimal number of clusters corresponded to the maximum silhouette coefficient (Rousseeuw, 1987) calculated with a varying number of clusters in $\{2, 3, 4, \ldots, N_{sig}\}$, where N_{sig} is equal to the total number of gene signatures. Genes sets shared by KO-enriched or control-enriched signatures were denoted as *meta-signatures* to distinguish them from the cell cluster-specific signatures, and defined as the average of the signatures belonging to the same cluster. Genes defining the KO-enriched or control-enriched *meta-signatures* were finally analyzed by GSEA to identify affected pathways.

Pathway-score estimation

Pathway scores of fitness and stress signatures were estimated as the first principal component scores of the cell cycle corrected counts of the whole dataset, comprising all cell populations and time points. Only detected genes that belong to the relevant Hallmark gene sets in the MSigDB database were used for the estimation of the principal components.

Transcriptional burst analysis

Burst kinetics were estimated using the approach described in (Larsson et al., 2019). A two-state model of stochastic gene expression was assumed to estimate the parameters (frequency and size) of the transcriptional bursts. In this model, each gene is characterised by a state (i,n), where $i \in \{0,1\}$ indicates whether the gene is in the ON or OFF state, respectively, and n represents the raw counts of RNA transcripts in each cell. The stationary state, derived from the model introduced in Peccoud et al., (Peccoud and Ycart, 1995) can be described by a Poisson-Beta process:

$$p|k_{on}, k_{off} \sim Beta(k_{on}, k_{off})$$

$$n|k_{syn}, p \sim Poisson(k_{syn} * p)$$

where k_{on}, k_{off} represent the genes ON, OFF rates, while k_{syn} represents the transcription rate when the gene is in the ON state. Burst frequency is represented by k_{on} and burst size bs is defined as the ratio k_{syn}/k_{off}. While a two-state model likely does not capture all the variables affected by the complex biological perturbation induced by nutrient deprivation, (Tunnacliffe and Chubb, 2020) we assumed that pairwise comparisons between cell populations are not affected by possible approximations. The three k parameters were estimated for each cell population at each time point, separately, using the code available at https://github.com/sandberg-lab/txburst (version of the code available in September 2020). All parameters were estimated using the raw RNA counts. As indicated above, technical variability across samples was minimal. Maximum likelihood (ML) inference was used to obtain the parameters as described in Larsson et al. While our dataset does not have allele resolution, any over- or under-estimation of the kinetics parameters equally affects all compared samples. This is particularly relevant as the aim of this analysis is not to estimate absolute kinetic parameters, but to semi-quantitatively assess relative changes across conditions. Furthermore, we have verified that burst parameters from two distinct alleles as estimated by Larsson et al. are highly correlated ($R^2 = 0.79$), indicating that estimates from the combined alleles do not substantially affect comparisons across conditions. HFGs were defined as genes with a $k_{on} > 4$.

ATAC-seq analysis

FASTQ files for each sample were processed via the nf-core/atacseq pipeline (Patel et al., 2022) against the *Homo sapiens* hg19 genome build with the following parameters -profile crick –deseq2_vst –fasta –macs_gsize 2.7 × 10^9 –bwa_index –min_reps_consensus 1. This produced the BigWig files used for subsequent analysis. Heatmaps and metaprofiles at gene promoters and active enhancers were generated using deepTools: (Ramírez et al., 2016) the computeMatrix function was used against the BigWig files for each sample to provide a matrix of the density of chromatin accessibility with the following settings: 'reference-point –referencePoint = TSS –sortRegions keep –metagene –missingDataAsZero -b 1000 -a 1000 -bs 10'. Subsequently, these matrices were plotted with plotHeatmap with the settings –sortRegions keep –missingDataColor 1 –zMax 3 –yMax 3'. Additionally, the density of ATAC signal in each list was explored using plotProfile using the settings: '–yMax 3'. For correlation scatterplots and comparison of peak distributions by boxplots, cumulative RPKM values over a 2Kb window centered on promoters or active enhancers were retrieved from the deepTools compute matrixes. Fitness and stress genes were defined as genes belonging to the identified GSEA signatures (Figure S4B) and that showed early differential expression in control cells (d2 vs d0, FDR <0.01).

ChIP-seq analysis

FASTQ files for each sample were processed via the ChIP-seq pipeline v1.2.2 (Patel et al., 2021) available at nf-core against the *H. sapiens* hg19 genome using the –broad option for MACS to identify broad peaks for H3K27me3 and the –narrow_peak option for H3K27Ac, H3K4me3 and H4K4me1. This produced the BigWig files used for subsequent analysis. Metaprofiles at fitness and stress gene promoters were generated using deepTools: the computeMatrix and plotProfiles functions were used against the BigWig files for each sample to provide a matrix of the density of ChIP signal and generate metaprofiles in a 5Kb window centered on gene TSSs. For quantification of differential peaks, the DESeq2 output of the nf-core pipeline was further analyzed to eliminate peaks of unlikely biological significance: detected peaks were first filtered based on magnitude, retaining regions with pseudo-counts $\geq$ 250 in at least one sample (maximal value: 25,035). The fraction of differential peaks (FDR <0.01, log2 FC $\geq$ 1 or $\leq$1) was then calculated, assessing either all peaks genome-wide or peaks at promoters of fitness and stress genes. Promoter regions were identified using the nf-core pipeline default annotation method. Fitness and stress genes were defined as stated in the ATAC-seq section.